Master of Science Thesis

Investigation on inviscid flow methods for 2D LEI tube kite

P.S.M. Mandru

23^{rd} February, 2018

Faculty of Aerospace Engineering · Delft University of Technology

Investigation on inviscid flow methods for 2D LEI tube kite

Master of Science Thesis

For obtaining the degree of Master of Science in Aerospace Engineering at Delft University of Technology

P.S.M. Mandru

23^{rd} February, 2018

Faculty of Aerospace Engineering · Delft University of Technology

Delft University Of Technology
Department Of

The undersigned hereby certify that they have read and recommend to the Faculty of Aerospace Engineering for acceptance a thesis entitled **"Investigation on inviscid flow methods for 2D LEI tube kite"** by **P.S.M. Mandru** in partial fulfillment of the requirements for the degree of **Master of Science**.

Dated: 23^{rd} February, 2018

Supervisor: _____
Dr.ing. Roland Schmehl

Supervisor: _____
Dr.ir. Carlos Simao Ferreira

Reader: _____
Dr.ir. Alexander van Zuijlen

Summary

On a typical 2D LEI kite profile, flow separation is expected to occur on both suction and pressure sides of the airfoil. This thesis is aimed to study various inviscid flow models that are capable of modeling such multiple flow separation phenomena.

Inviscid models are capable of modeling single flow separation region over typical airfoils. In these models, the flow separation is modeled by releasing vorticity in to the flow from the separation location which are known prior and given as a direct input to the model. The separation locations can be taken either from experimental data or RANS simulation results of the airfoil. From the various singularity elements available for modeling, in this thesis point vortex elements and linear distribution of vorticity elements are utilized for modeling the flow and a step by step procedure of development of the solver starting from steady state to unsteady single wake and then to double wake model is followed. Each solver developed is validated against available analytical results. However, in the time line of the current study, the double wake model developed could not be validated with the chosen test case. The modeling challenges faced in the development phase of double wake model can be mainly attributed to the unclear modeling details in implementing the strength of the separation vortex that is shed from separation location. The other challenged include accumulation and crossing of shed wake elements through the airfoil surface, similar to the challenges reported by Rachel [25]. These challenges are clearly discussed and recommendations have been made for overcoming wake shedding problem.

The author believes that such an inviscid model overcoming the modeling challenges experienced in double wake model, can be easily extended to model multiple separation regions over 2D LEI tube kites.

Acknowledgements

My sincere thanks to Prof. Roland Schmehl, who is responsible for my first encounter to the technology of airborne wind energy. I received the first edition book on airborne wind energy during bachelor thesis from Prof. Schmehl, which inspired me to pursue masters at TU Delft. I have attended AWEC 2015 conference where I got listen to his presentation and got a chance to exchange ideas about the technology, and this filled passion to work at Kite Power research group. Thank you very much for spending time, energy with me in spite of your busy schedule. I had great fun discussing and sharing thoughts on the technology during days of my assistantship. Thank you for all the support and encouragement during the time of thesis work.

Thank you to Prof. Carlos Simao Ferreira for guiding me through the course of thesis work and taking interest in the project with out any obligation. I really enjoyed discussing the project during our meetings and I truly wish to have spent more time with you. I want extend my gratitude to PhD candidate Rachel Leuthold whose thesis work inspired me to carry out research in this area of vortex methods. I am very thankful for taking time out ans showing utmost interest during our discussions.

Thank you to all my lab mates especially Andres and Chinmey for such a wonderful atmosphere in the lab and being with me through the stressful times. Special thanks to Andres for the times we spent on our common interest, music and your humor which I enjoyed a lot and this helped me to keep focusing on the project even during the days when I was stuck with out much progress. Thank you to all my friends especially Aji, Vivek, Harshil, Arun, Sai, Piyush, Adha, Gole, Harshad, Vaibhav, Vishaal for being there and attending all my concerns with patience and helping me get through difficult times. Thank you Sajjad Ahmed for allowing me to stay at your place and sharing your sense of respect and responsibility towards fellow human beings.

I want to thank my parents for their immense trust, understanding and unconditional love without which I wouldn't be the person I am today. Thank you for all the encouragement.

Thank you.

Delft, The Netherlands — P.S.M. Mandru
23^{rd} February, 2018

Contents

List of Figures

List of Tables

Chapter 1

Introduction

Airborne wind turbines are a new class of wind energy harvesters that extract power from high altitude wind. The airborne wind energy (AWE) technology will replace the tower or mast involved in conventional wind turbines (CWT), by a tether which connects kite to the ground. This tether would be reeled out, as it would be pulled by aerodynamic force generated by kite, to reach high altitudes tapping the highest density source of renewable energy. Different kites with various shapes and materials are possible, from fixed wings like a glider airplane to completely soft (flexible) wings as used by surfers. This kite is equivalent of the wing tips of CWT. It will fly in circles or figures of eight to increase the effective wind speed. By the removal of heavy components from the system of CWT, makes AWE power plant much more flexible in terms of location, and considerably cheaper in construction. At present, different airborne devices are utilized to harness power from high altitudes using different engineering principles (on board to ground based power generation). The structural limits of conventional wind turbines restricts reaching higher altitudes. Also with increasing height, in order to reach high altitude winds, the costs for the tower involved in CWT increase exponentially and require a sophisticated infrastructure for transporting the heavy components and assembling the power plant. However AWE overcomes the conventional restrictions and enables production of high efficient, low cost energy. This technology is currently under investigation by several researcher groups at universities and start-up companies.

There are many shapes of sail wings which have been subject to aerodynamic analysis in order to mimic flow around and estimate pressure distribution, since last century. Depending on the shape of sail-wing, the flow characteristics vary as discussed below. Here the study is driven towards the interest of gathering information about flow characteristics at various angle of attacks on sail-wings in general and LEI tube kite used by TU Delft Kite Power Team, figure 1.1 in particular, that are vital for modeling. Experimentally measured data of aerodynamic characteristics of sailwings available for correlation is presented in Leuthold's thesis [25]. Several varieties of airborne wind turbines are realized in the last decade to extract energy from wind in different ways [8]. Current technologies include on board power generation, using a rigid aircraft structure, interest of Google's Makani Power company [18] and generation at ground station by Kitemill AS

Figure 1.1: One of the LEI kites designed and used by the TU Delft AWE group for power-generation.

[16], Ampyx Power B.V [17], Enerkite GmbH [11]. Here at TU Delft, KitePower research group [19] focuses on producing energy at a ground generator run by surf kite/parachute like structure [8].The goal of thesis is to develop a robust aerodynamic model that meets the requirements of fluid structure interaction FSI study. An accurate FSI model is capable of providing an insight into design methodology of kites depending on the requirement. Such model can be economical as it reduces the initial design evaluation time of required kite by eliminating capital involved in the construction and conduction of field tests. Hence, the author realizes that a robust aerodynamic model is a vital part of design methodology for achieving required FSI model.

The information in this report is divided into chapters that provide the following details in the given order.

- Chapter 2: provides necessary literature for understanding the flow over 2D LEI tube kite by correlating with common flow behavior over mast/sail wings. Brief review on available aerodynamic models for LEI kite and various relatable inviscid flow models for modeling flow separation that are available in the literature
- Chapter 3: deals with necessary theory that governs the incompressible, inviscid and incompressible flow for the development of intended aerodynamic model
- Chapter 4: gives a detailed description of the computational information involved in the development of inviscid steady and unsteady flow models
- Chapter 5: provides validation for each of the models developed and discusses the modeling challenges faced in the double wake model developed
- Chapter 6: conclusion of the results obtained in the study
- Chapter 7: gives recommendations for overcoming few modeling challenges that are faced during the development phase of double wake model

Chapter 2

Literature Review

This chapter briefly provides the literature study conducted during the course of the thesis. To identify the requirements of desired computational model, the characteristics of the flow over a typical 2D LEI kite profile have to be understood. For this purpose, the flow over typical sail wing is studied and the expected flow behavior on a typical 2D LEI kite profile is presented in section 2.1.

The aerodynamic models available and study conducted on 2D LEI kite geometry and 3D wing are presented in section 2.2. Comparing the lift polar of typical 2D LEI kite airfoil obtained from Breukels to a typical airfoil lift polar, the type of stall prone to occur on a 2D LEI kite profile is discussed in section 2.3 and study is proceeded towards the inviscid models available in literature that capture such a flow separation or stall behavior.

2.1 Sail-wing aerodynamics

Several shapes of sail wings are subject to wind tunnel experiments [10],[7] and certain common flow behaviors are observed. Wilkinson [37] has performed wind tunnel tests over two-dimension sail-wings with masts of circular cross section, as shown in figure 2.1 for various geometric parameters in order to get insight into the fundamental nature of flow field existing over them. A universal form of pressure distribution was concluded after studying a entire 216 test results. The pressure distribution attributed to various regions on the sail-wings with circular mast is shown in figure 2.1, and the corresponding regions are identified in the table 2.1.

The effects of geometric parameters such as mast diameter to chord ratio, sail camber and flow parameters Reynolds number, aerodynamic incidence on the pressure distribution is studied. He found that change in Reynolds number has no effect on the pressure distribution.

Bailey [3] has developed a viscous-inviscid interaction method that couples a potential flow solver with integral boundary layer calculations to determine aerodynamic loads on

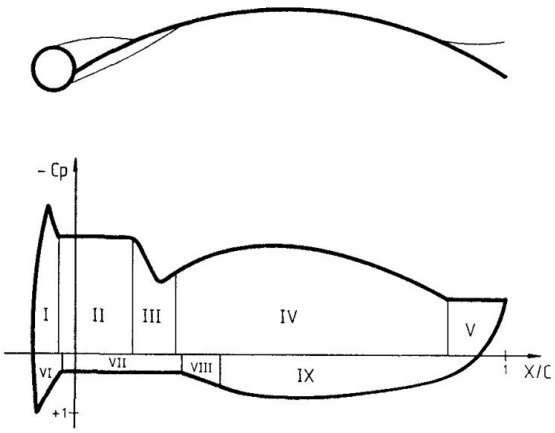

Figure 2.1: Universal pressure distribution over 2D mast/sail wings, as reproduced from [37]

Region	Description
1	Upper mast attached flow region
2	Upper separation bubble
3	Upper reattachment region
4	Upper aerofoil attached flow region
5	Trailing edge separation region
6	Lower mast attached flow region
7	Lower separation bubble
8	Lower reattachment region
9	Lower aerofoil attached flow region

Table 2.1: Description of various regions of universal pressure distribution on 2D mast/sail-wings, [37]

2D yacht sail rig configurations, as shown in figure 2.2. The pressure distribution results obtained for a foresail are validated and calculations are performed for mast and mainsail configurations. The flow characteristics of yacht mast/sail configurations are identified

Region	Description
1	Laminar boundary layer flow from stagnation on the mast and windward side of the foresail
2a	A leading edge separation bubble on the foresail
2b	Upper reattachment region
3	Separation bubbles from the rear of the mast with turbulent reattachment on the mainsail
4	Possible turbulent separation ahead of the trailing edge

Table 2.2: Characteristics of flow over 2D yacht mast and sail configurations, [3]

in table 2.2 and corresponding regions are indicated in figure 2.2.

Considering a typical 2D LEI tube kite airfoil profile, as shown in figure 2.3, we can expect similar flow behavior. On the upper surface (suction side), a formation of separation

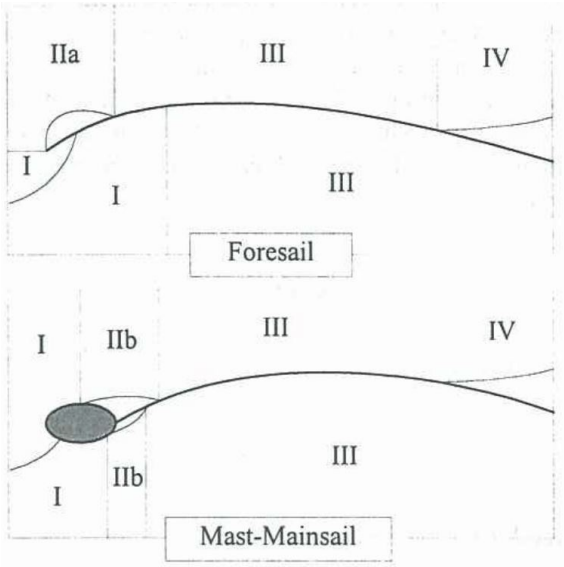

Figure 2.2: Regions around 2D yacht rig configurations, as reproduced from [3]

bubble behind the tube is not obvious since canopy is smoothly attached to the LE tube. On the lower surface (pressure side), a similar separated flow is expected because the significant effective cavity present behind the mast but flow reattachment is not obvious although flow transition is plausible. And at high angle of attacks, a similar flow separation and reattachment (separation bubble) can be formed. Also, trailing edge flow separation is expected to occur but it is influenced by the camber of canopy. Table 2.3 summarizes all the expected flow behavior over a 2D LEI tube kite airfoil profile.

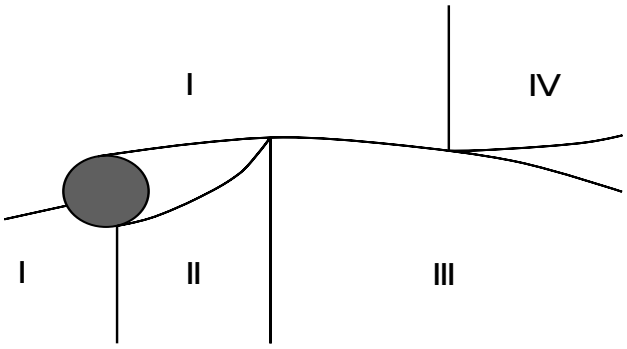

Figure 2.3: A typical 2D LEI tube kite airfoil profile.

2.2 Aerodynamic analysis models

Literature survey reveals that the available aerodynamic models are either fast or accurate and do not meet the requirements of FSI modeling. Breukels model (BAM) was one of advanced aerodynamic models in AWE field to estimate 3D forces on kite [6]. In BAM, the aerodynamic loads on the kite are approximated using finite strip theory which doesn't account for the three dimensional flow behavior over the kite. According to

Region	Description
1	Laminar boundary layer flow from stagnation point on the LEI tube, attached flow region on LEI tube
2	A pressure surface flow reattachment region
3	Separation bubbles from the rear of the LEI tube with turbulent reattachment on the canopy
4	Possible turbulent separation ahead of the trailing edge on the suction surface

Table 2.3: Characteristics of flow over typical 2D LEI tube kite airfoil.

finite strip approach, the loads on the wing are determined by appropriate summation of loads over individual finite number of spanwise elements. Since the wing has different spanwise sections with different shape, he came up with the idea of forming a polynomial fit for aerodynamic characteristics based on geometric properties that define shape of the airfoil. The parameters that define the shape of the 2D airfoil profile are chord length c, camber $k = \frac{b}{c}$, thickness $t = \frac{d}{c}$, as shown in figure 2.4. The inaccuracy of this model can be attributed to correction methods used in order to arrive at 3D aerodynamic coefficients from 2D airfoil computational fluid dynamics (CFD) data. Also BAM converts the pressure to nodal loads by using empirical weight functions which should be known before hand as it is dependent on 2D airfoil shape.

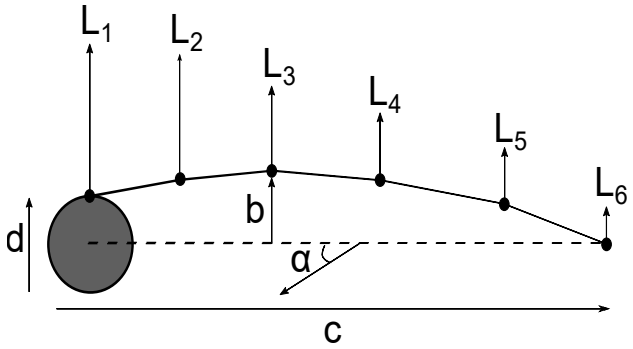

Figure 2.4: A schematic representation of LEI tube kite - 2D airfoil profile - BAM [6].

The CFD analysis performed by Breukels on three sets of airfoils with different thickness 15%, 20%, 25% and each thickness set has airfoils ranged in camber from 0% to 12% showed that even at 0 deg angle of attack, a considerable amount of turbulent intensity is present around the airfoil most of which is concentrated on the pressure side, as shown in figure 2.5. At 8 deg angle of attack, in addition to pressure side, there is an increased turbulence intensity at the trailing edge of the suction side. This indicates airfoil falls into trailing edge stall category. However flow also separates at the leading edge on the pressure side, which is a new flow separation scenario that is not dealt in typical aerodynamic airfoils analysis. Unsteady analysis at 20 deg angle of attack revealed the formation of Von Karmann vortex street as in the case of any flat plate or airfoil but there is an additional flow separation shear layer emanating from leading edge and from figure 2.6, it is evident that this separated flow reattaches at the trailing edge. This is clearly evident from turbulent intensity contour video of unsteady simulation of a typical

tube kite airfoil at 26 deg angle of attack.

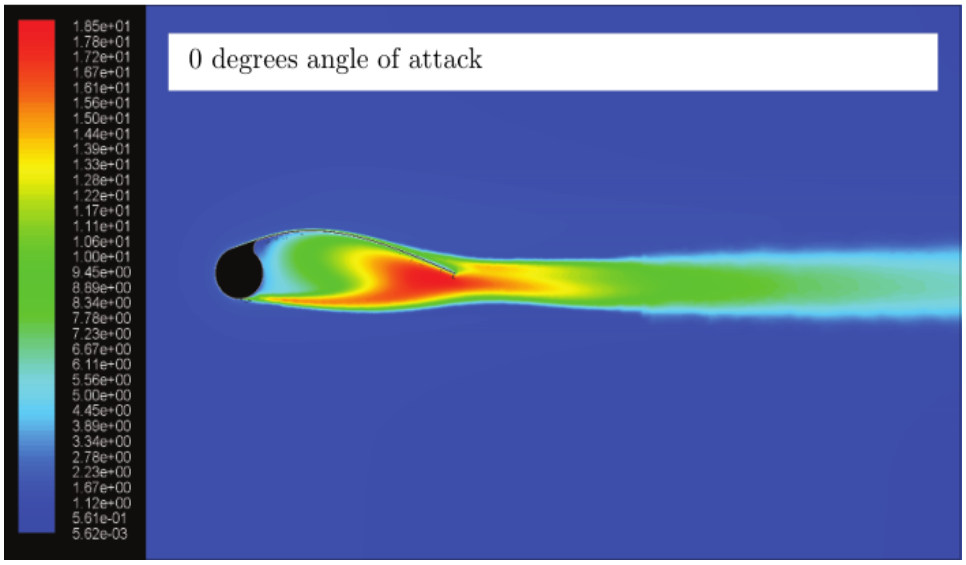

Figure 2.5: Plot of turbulence intensity at 0 degrees angle of attack, as reproduced from Breukel's Ph.D. thesis [6].

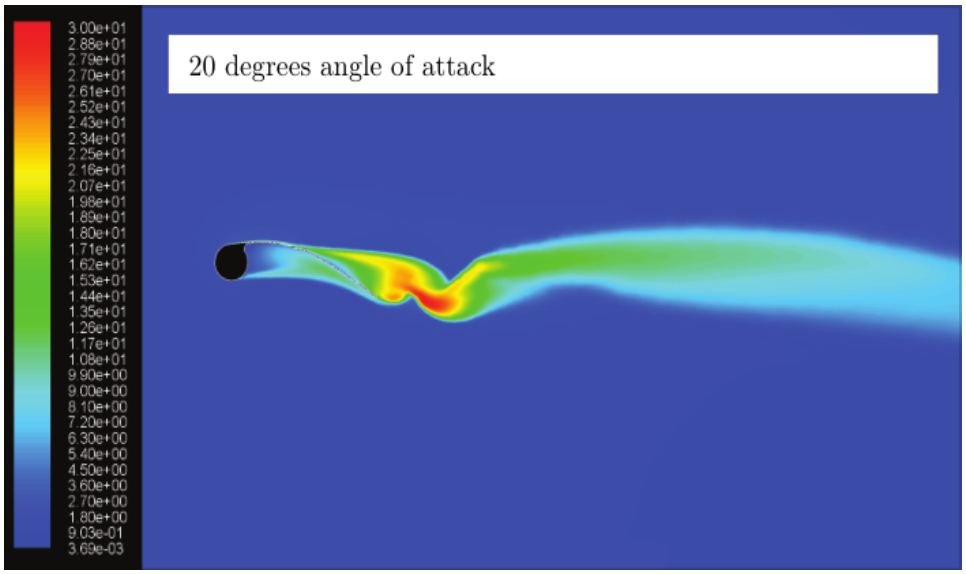

Figure 2.6: Plot of turbulence intensity at 20 degrees angle of attack, as reproduced from Breukel's Ph.D. thesis [6].

The aerodynamic characteristics obtained from CFD analysis are fitted using to appropriate polynomial functions of thickness and angle of attack. In the range of -20 deg to 20 deg angle of attack, the lift coefficient is approximated using third order polynomial of angle of attack, shown in figure 2.7. From the lift polar, figure 2.7, it can be noticed that there no sudden drop in lift coefficient indicating a trailing edge type stall where flow starts separating at trailing edge at moderate angle of attacks. The flow separa-

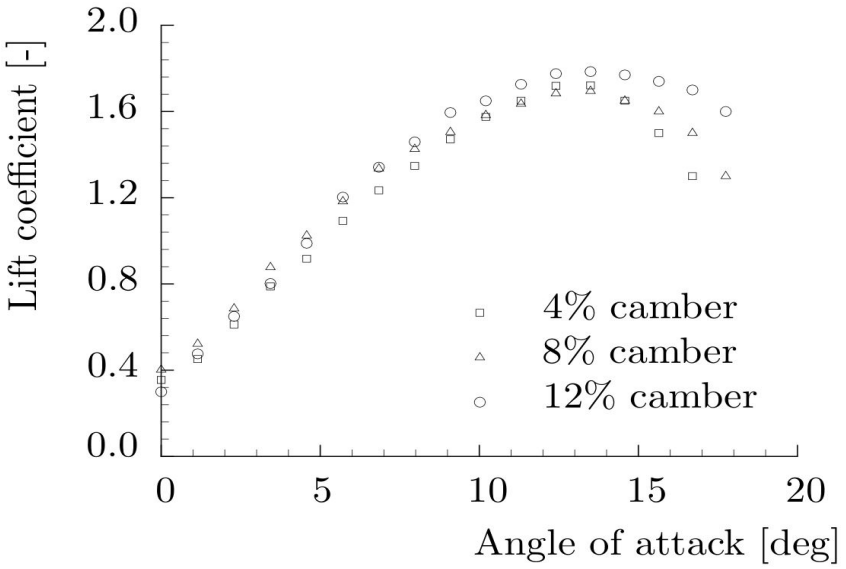

Figure 2.7: C_L - α curves for a 15% thick sail wing airfoil at different values of camber, as reproduced from Breukels [6].

tion location slowly reaches leading edge at $\alpha_{C_{L,max}}$. And as camber increases, $C_{L,max}$ is increasing.

Bosch [2] and Mandru & Jadhav [31] developed quasi-steady FSI models using Breukels model as aerodynamic input. If not BAM, these models could be robust enough to be used for iterative design process. A non linear vortex lattice method proposed by van Kappel (VLM_{N-VK}) [34] is proved to be relatively accurate compared to Breukels method because this model is based on VLM which incorporates effects of finite wings and has a higher flexibility in predicting chord-wise pressure distributions. This computation model is fast and simple relative to Breukels model but its real time factor of 1100x is too slow with respect to FSI coupling which makes is less attractive for iterative design. The accuracy of this model boosts confidence that vortex panel/lattice methods are capable of modeling kite aerodynamics.

Leuthold [25] modeled kite aerodynamics using a time dependent multi-wake vortex lattice method (VLM_{MW-RL}) and found that the computational effectiveness and accuracy is heavily limited by the methods inability to model reattachment. When the already separated flow on the pressure side and separation vortex lattice comes closer to the bound vortex lattice, there was a overshoot of velocity induced on the separation vortex lattice passes through the bound vortex, as shown in figure 2.8. Leuthold also proposed alternative modeling option (double-wake method) which is promising but application of alternate proposal is subject to discussion. Keeping the requirements of aerodynamic model proposed by Leuthold intact [25]], the main goal of this thesis is to develop a suitable time dependent vortex (panel/ discrete vortex) method with appropriate source distributions such that it overcomes the limitations of VLM_{MW-RL}.

Micheal Deaves [9] performed steady state 3D RANS analysis of LEI tube kite with smoothed profiles, as shown in figure 2.9. He found that there is always pressure surface separation at the leading edge even in normal operating conditions. On the suction-

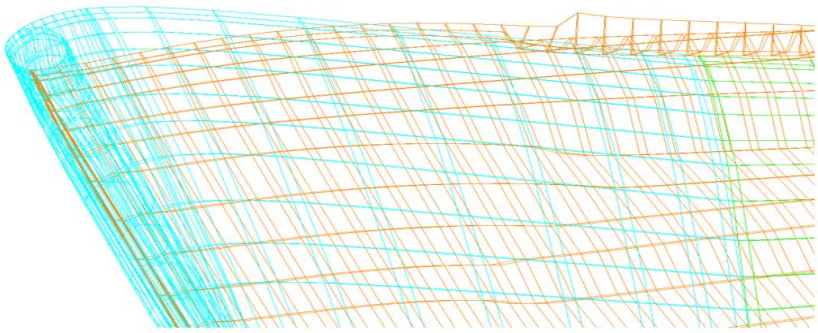

Figure 2.8: The reattachment problem as the pressure-surface separation vortex lattice passes through the bound vortex lattice at $\alpha = 0\,\mathrm{deg}$, as reproduced from Leuthold's M.Sc. thesis [25].

surface, it appears that separation begins at tip region of the kite at around 16 deg angle of attack and this position varies along spanwise locations of the kite. There is no consistent way to predict these separation locations on suction-surface along the span, and also the separation line is discontinuous.

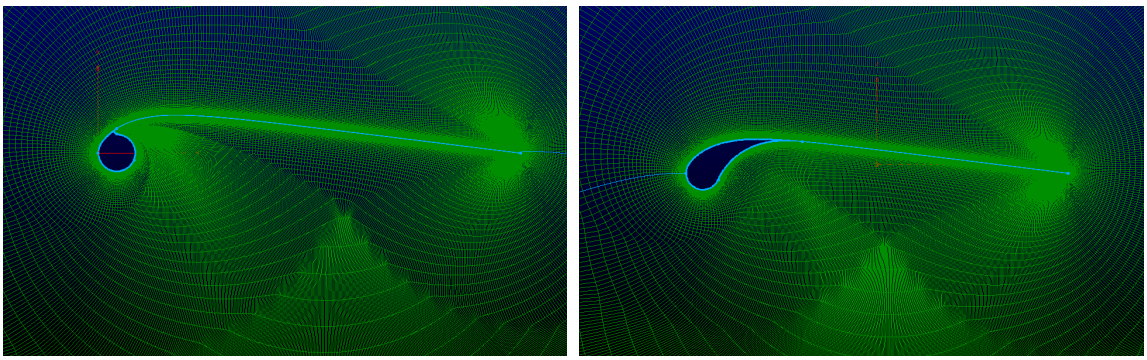

Original profile Smoothed profile.

Figure 2.9: Meshes generated to investigate the effect of smoothing behind the leading edge tube, as reproduced from Deaves's M.Sc. thesis [9]

Leloup [24] calculated the loads on a 3D wing by distributing the span wise loads obtained from 2D XFOIL using LLT and validated this approach for curved paraglider wings but only for the range of angle of attacks for which flow is fully attached. This 3D LLT couldn't capture the flow separation phenomenon and is restricted in validity to angle of attacks between $-10 < \alpha < 10$, linear region of $C_L - \alpha$ curve.

2.3 Inviscid flow models

A theoretical understanding of vortex methods possible with (combination of) various kinds of singularity element distributions available in the literature is necessary. A critical overview on the possible time dependent behavior (modes) of the kite is needed and a decision on extent of time dependency required for modeling purpose is necessary.

Leuthold [25] has considered various possible modes (including sub-scale deformation modes) of kite and found that quasi-steady assumption is convincing for FSI problem when sub-scale deformation modes are neglected. The author understands that sub-scale deformations are a part of FSI problem and since the interest is to develop a quick model to estimate aerodynamics forces on a fixed kite geometry. Later these aerodynamic forces are transfered to a structural model using appropriate coupling techniques [29]. However our model should be able to capture (which is implied objective) the difference in aerodynamic forces due to small deformations when run iteratively in order to fulfill requirements of FSI study.

The cross section of a simple sail-wing, is a cambered flat plate as shown in figure 2.10. Subject to different angle of attacks, flow over such sail-wings exhibits similar behavior to that of an airfoil. It is expected that the flow separates at certain angle of attacks and this process depends on various equivalent factors that are identified for an airfoil. The lift coefficient of airfoil increases with increase in angle of attack only till a certain value, after which lift drops due to flow separation. The term stall is used to describe this phenomenon of drop in lift [33]. The flow separation phenomenon is governed by parameters defining the shape of airfoil such as camber, thickness and Reynold's number, free stream turbulence, roughness etc. There are three principle types of stall recognized [33], [28] such as

- trailing edge stall, initiated when the boundary layer starts to separate close to trailing edge at certain angle of attack and this separation location moved forward, towards leading edge with increase in angle of attack. In this process, the lift loss is rather gradual.
- leading edge stall, initiated abruptly at certain angle of attack where the flow separates from the leading edge and lift drops suddenly, in contrast to trailing edge stall,
- thin airfoil stall, initiated at certain angle of attack when the flow separates at the leading edge and reattaches farther downstream of the airfoil forming a separation bubble. This reattachment point moves downstream with increase in angle of attack, increasing the length of separation bubble. When the reattachment point reaches the trailing edge.

In a general sense, the figure 2.11 represents the effect of various flow separation phenomenon on the lift coefficient of a airfoil. Trailing-edge stall occurs for airfoils having thickness to chord ratio $(\frac{t}{c})$ is greater than 0.15, leading edge stall occurs when $0.15 < \frac{t}{c} < 0.09$ and thin airfoil stall for $t/c < 0.09$, [33].

McCullough and Gault have studied different airfoil sections to understand the role of boundary layer flow and separation phenomenon for various stall cases [28]. Intensive wind-tunnel experiments on five symmetrical airfoil sections showed that stall behavior of every airfoil section cannot be simply categorized to one of the stall groups based on thickness information. Also, there can be a combination of According to their study, flow separation is mainly related to the boundary layer growth which is influenced by factors such as Reynolds number, free stream turbulence, surface roughness and pressure gradient. Variation in any of these factors can change the stall of a given airfoil from one

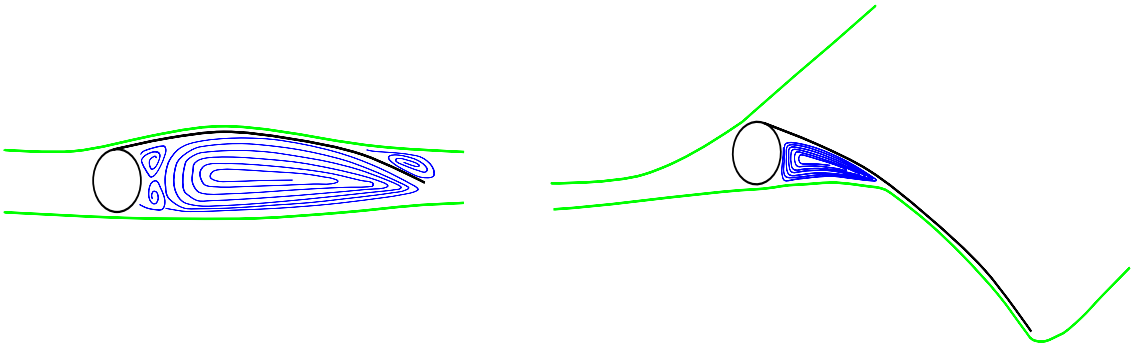

Figure 2.10: Concept sketch of flow over 2D LEI tube kite airfoil at moderate and high angles of attack.

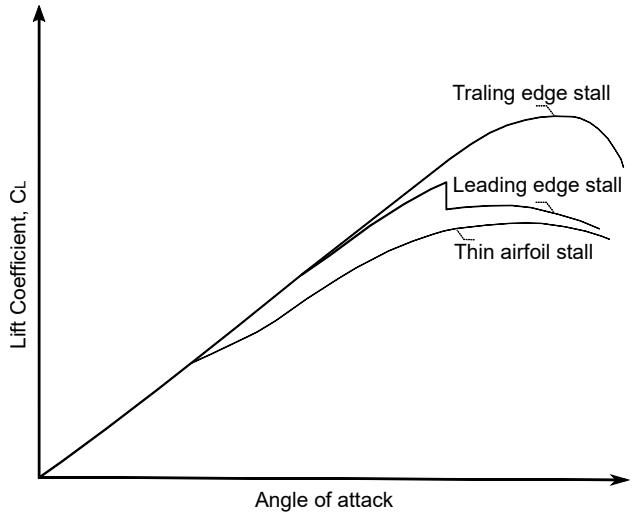

Figure 2.11: Lift polar behavior for various types of stall, as given in [33].

type to another. But for most practical airfoil sections, trailing edge stall is characteristic type of stall for thick airfoils. In the case of appearance of separation bubble (thin airfoil stall), increase in angle of attack at a given Reynolds number increases the extent to separation bubble due to which the thickness of turbulent boundary layer formed past the separation bubble increases. This growth in the thickness of turbulent boundary layer facilitates flow separation (trailing edge stall) [36]. And an increase in Reynolds number decreases the extent of laminar separation bubble region and hence thickness of farther turbulent boundary layer.

Potential flow theory is widely accepted and used to mimic several complex flow phenomenon including unsteady aerodynamics. When the viscous effects are confined to thin boundary layers, potential flow theory has been extensively used to determine the aerodynamic characteristics of two dimensional airfoils. But when the boundary layer becomes thick or separates, classical potential theory must be modified to account for the vorticity being released into the flow [20].

Joseph Katz [22] has developed a discrete vortex model based on thin airfoil theory to analyze separated flow over a cambered airfoil. The vorticity released at the separation

locations is also modeled using discrete vortices, as shown in figure 2.12 The location of separation point in this model was an input from experimental or flow-visualization data. The strength of two shear layers (one at flow separation location and the other at

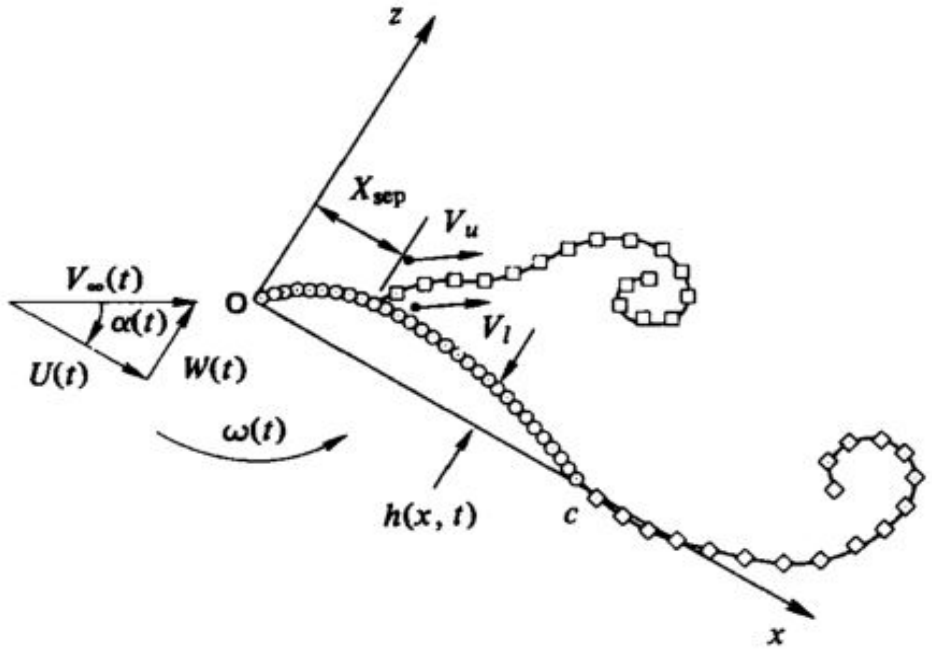

Figure 2.12: Schematic description of model, as reproduced from [22]

trailing edge) emanating is calculated by performing the line integral of velocity along an enclosed portion of the wake behind the separation location. Considering a closed line integral around the separation shear layer as shown in figure 2.13,

$$\frac{d\Gamma_S}{dt} = \frac{D}{Dt}\oint V ds \tag{2.1}$$

$$= \frac{d}{dt}(V_U ds - V_L ds) \tag{2.2}$$

$$\cong \frac{1}{2}({V_U}^2 - {V_L}^2), \tag{2.3}$$

where Γ_S is separated wake vortex circulation strength. A good agreement in the post-stall aerodynamic data of two airfoils NACA 0012 and NACA $63_2$415 was established. Also calculated Strouhal number of periodic wake oscillation due to separated flow over flat plate is in close agreement with experimental results [12]. He also developed a VLM, using the same approach, for locally separated flow over wings and validated the lift coefficients for a rectangular planform (section: NACA $63_2$415) having aspect ratio of 7.5 at Reynolds number 1.5 million [21].

It is learnt from literature study that Kutta condition is not unique but needs to be formulated for each mathematical model. Hess and smith [15] used equal velocities at upper and lower trailing edge panels as Kutta condition in case of steady state analysis. Basu and Hancock [4] has argued that there is a different Kutta condition which is time dependent but is derived with the same underlying principle of zero loading at the trailing

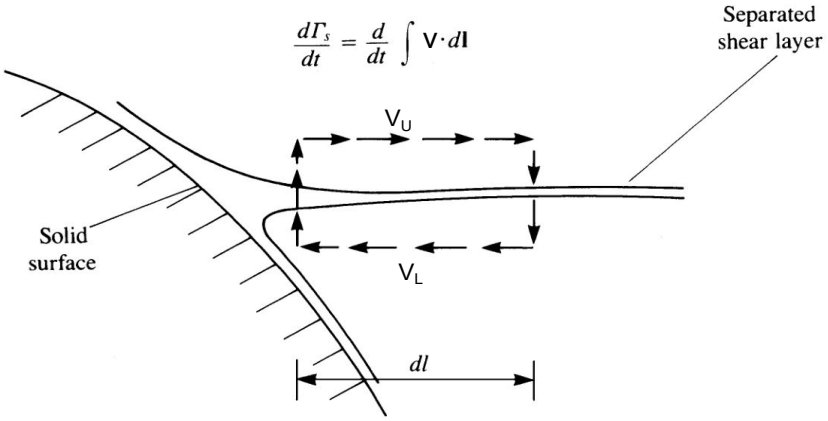

Figure 2.13: Calculating vorticity shed at separation location, as reproduced from [23]

edge at all times. They have developed a numerical method using uniform strength source and vortex panels as singularity elements, as shown in figure 2.14.For steady state calculations they used the kutta condition of equal tangential velocities at the trailing edge. panels. They also calculated the pressure distribution on a two dimensional airfoil

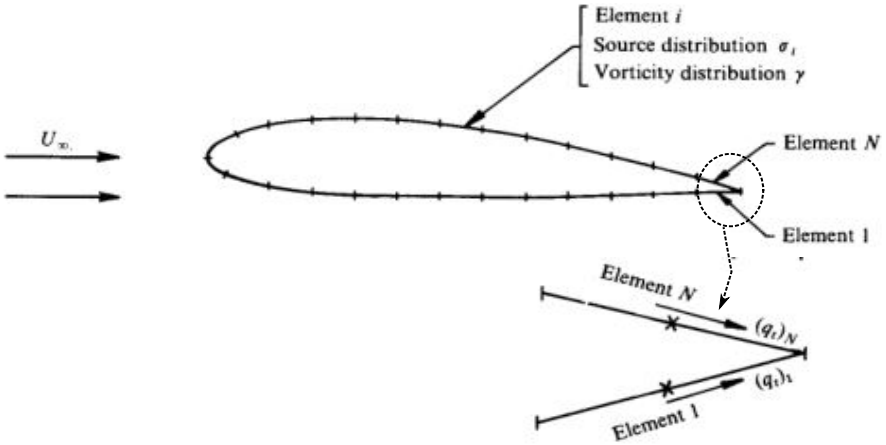

Figure 2.14: Description of steady state model by Basu and Hancock, as reproduced from [4]

undergoing an arbitrary unsteady motion in an inviscid incompressible flow. The time dependent Kutta condition results in non linear equation with respect to strength of shed vortex. Using the unsteady Bernoulli's equation and applying the condition of equal pressures at midpoint of two elements at the trailing edge of airfoil, as shown in figure 2.15, a time dependent kutta condition is obtained.

$$\frac{\partial \phi_N}{\partial t} - \frac{\partial \phi_1}{\partial t} + \frac{{q_t}_N{}^2 - {q_t}_1{}^2}{2} = \frac{p_1 - p_N}{\rho}$$

We know, from [20]

$$\frac{\partial \phi_N}{\partial t} - \frac{\partial \phi_1}{\partial t} = \frac{\partial \Gamma_k}{\partial t}$$

Applying zero loading at trailing edge condition, we get

$$\frac{{q_{t_1}}^2 - {q_{t_N}}^2}{2} = \frac{\Gamma_k - \Gamma_{k-1}}{t_k - t_{k-1}} \tag{2.4}$$

The length and angular orientation of shed panel is initially guessed and are updated iteratively till convergence, as given below.

$$\tan\theta_k = \frac{W_{wk}}{U_{wk}}$$
$$\Delta_k = [U_{w_k}^2 + W_{w_k}^2]^{\frac{1}{2}}[t_k - t_{k-1}].$$

Their model showed satisfactory results for symmetrical Von Mises 8.4% thick airfoil under various unsteady motions such as

- a sudden change in airfoil's incidence,
- an airfoil oscillating at high frequency,
- an airfoil passing through a sharp edged gust.

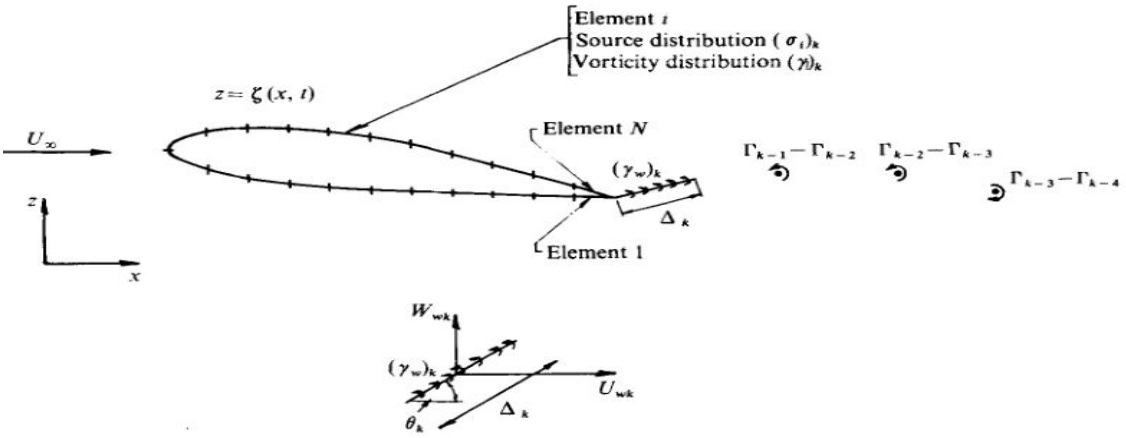

Figure 2.15: Description of unsteady model by Basu and Hancock, as reproduced from [4]

Vezza and Galbraith [35] presented a new method to capture unsteady flow over an airfoil with upper surface flow separation. They used linearly varying strength vortex panels as singularity elements to represent the airfoil and two additional constant strength vortex panels, one at each separation location, as shown in figure 2.16. These separation vortices were convected as discrete point vortices when they are considerably away from airfoil. A unsteady motion of step change in the angle of incidence of airfoils NACA 23012 and NASA GA(W)-1 was modeled and achieved results of pressure distribution time history and steady state distribution shows good agreement with experimental results.

A unsteady vortex panel method by Alessandro Zanon [1] successfully modeled 2D NACA 0012 airfoil at various reducing frequencies (k) and validated the case $k = 0.05$ with PIV experiments. He modeled airfoil using the singularity elements - constant strength source and vortex panels and separation shear layers with constant strength vortex panels, shown

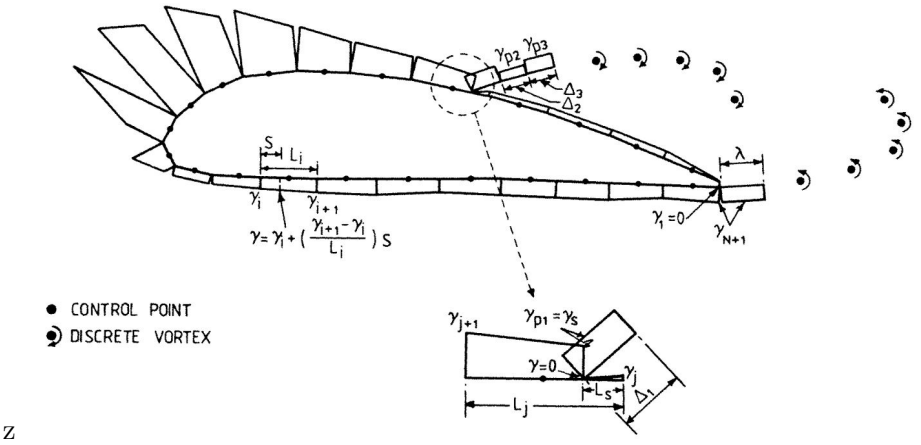

Figure 2.16: Unsteady flow separation model by Vezza , as reproduced from [4]

in figure 2.17. The wake is modeled using vortex blobs with a defined finite core radius. The unsteady kutta condition in his model is further linearized by the assumption of constant strength vortex panel, as mathematically elaborated below. Using the expression derived by Basu and Hancock derived 2.4

$$\frac{\partial \Gamma_W}{\partial t} = \frac{{q_{t_1}}^2 - {q_{t_N}}^2}{2},$$
$$\frac{\partial \Gamma_W}{\partial t} = \frac{(q_{t_1} - q_{t_N})(q_{t_1} + q_{t_N})}{2},$$
$$\frac{\partial \Gamma_W}{\partial t} = \gamma_W \Delta L = \frac{(q_{t_1} - q_{t_N})(q_{t_1} + q_{t_N})}{2},$$
$$\gamma_W = (q_{t_1} - q_{t_N}),$$
$$\Delta L = \frac{q_{t_1} + q_{t_N}}{2},$$

where γ_W is the circulation strength per unit length of the separated shear layer at the trailing edge and ΔL is the length of the separation panel. Hence the product $\gamma_W \Delta L$ gives the amount of vorticity shed in the time interval $t_k - t_{k-1}$. Recently, in 2015, Ramos [30] has developed a inviscid double wake model for stalled airfoil. In this model, airfoil is represented with singularity elements - linearly varying vortex panels and the wake using constant strength vortex panels. The wake shape is obtained iteratively from the initial conditions or initial assumption. Both the vorticity sheets are straight lines at the initial stage and are connected downstream at a common point, as shown in figure 2.18. And this shape updated by the solver to follow the separated streamlines. This study is focused on the deep stall region where separation is assumed to take place at the leading edge. The key parameter in this study is the wake length W_L which is defined as

$$W_L = W_F W_H,$$

where W_F and W_H stand for the wake factor and the wake height respectively. W_H is defined as the orthogonal distance between the stagnation point at the separation location and the trailing edge at the initiation step and W_F depends on the airfoil geometry and the angle of attack. Ramos extended this double wake model to simulate unsteady stalled

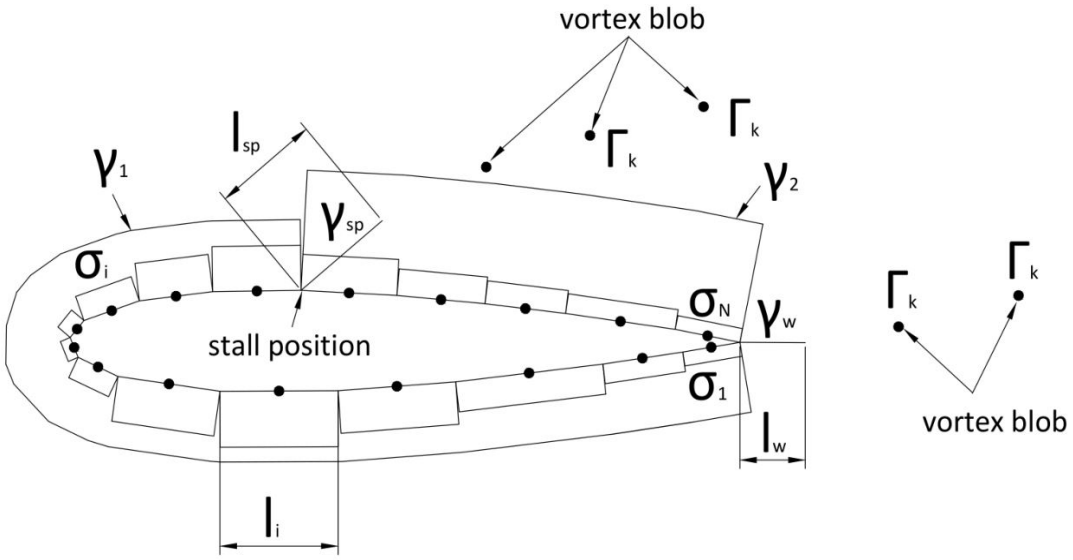

Figure 2.17: Unsteady flow separation model by Zanon , as reproduced from [1]

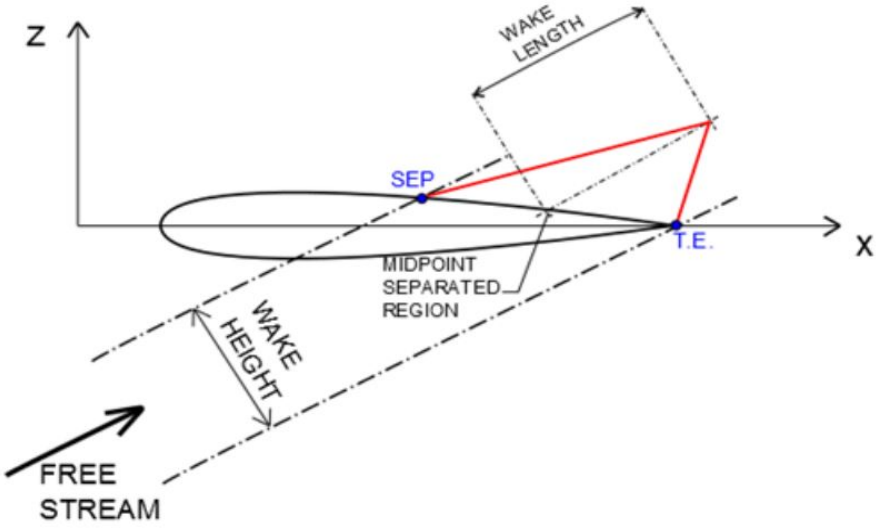

Figure 2.18: Steady state flow separation model of airfoil by Ramos, as reproduced from [27]

airfoils [32]. Here the difference can be mainly attributed to the boundary conditions and the modeling of the airfoil. Linearly varying vortex panels represented by the distribution of vorticity $\gamma_1, \gamma_2, \gamma_3, ..., \gamma_{N+1}$ and the two separated shear layers by constant strength vortex panels $\gamma_{w,SEP}, \gamma_{w,TE}$ with uniform strength source panels, σ are used as singularity elements. These form a total of $N + 4$ unknowns to be determined at a given time. The wake is modeled using vortex blobs. The vorticity released at the separation locations is estimated using from the panel just ahead of separation and the vorticity just after the separation location is zero, as shown in figure 2.19. The boundary conditions used to solve the system are as follows

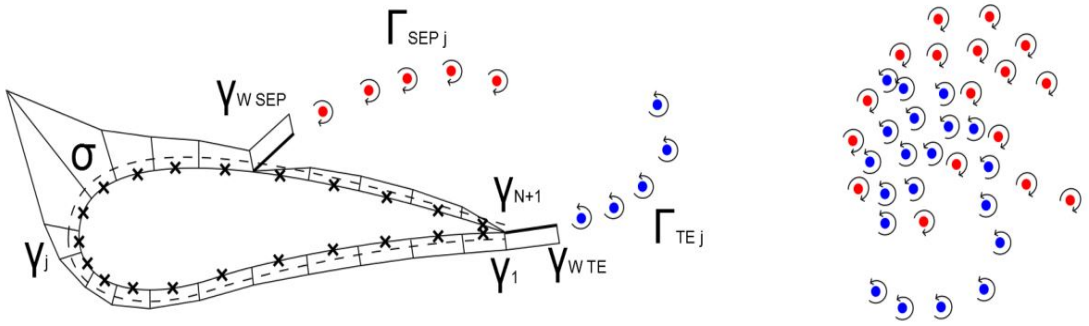

Figure 2.19: Unsteady flow separation model of airfoil by Ramos, as reproduced from [30]

- N: non-penetration condition applied at the center of each panel; $U_i \cdot n_i = 0$,
- N+1: Kutta condition at trailing edge; $\gamma_1 + \gamma_{N+1} = \gamma_{w,TE}$,
- N+2: vortex strength of separation panel is defined as $\gamma_{w,SEP} = \gamma_{SEP}$
- N+3: Kelvin's Helmholtz theorem application; $(\gamma_{w,TE}\Delta_{w,TE})^t + (\gamma_{w,SEP}\Delta_{w,SEP})^t = \Gamma_B^t - \Gamma_B^{t-1}$. Where $\Delta_{w,SEP}, \Delta_{w,TE}$ are the lengths of the separated vortex panels at separation location and trailing edge respectively.
- N+4: zero vortex strength at $N+1$, vorticity point at suction surface trailing edge panel end point: $\gamma_{N+1} = 0$

Here it is implied that $(N+3)^{rd}$ condition enforces the separation zone to start with a zero vorticity distribution, as shown in figure 2.19. This is applied indirectly, in the influence matrix by modifying the induction coefficients for the panel S.
In order to solve the non-linear equation of separation vortex strength [4], equation 2.4, an iterative procedure was followed by updating the length and orientation (angle) of the separation panels as

$$\Delta_{TE} = \frac{\text{mod } \gamma_{w,TE}}{2}, \tag{2.5}$$

$$\Delta_{SEP} = \frac{\text{mod } \gamma_{w,SEP}}{2}, \tag{2.6}$$

$$\Theta_{TE} = \begin{cases} \alpha_1 & \text{if } \gamma_{w,TE} < 0, \\ \alpha_{N+1} & \text{if } \gamma_{w,TE} > 0, \end{cases} \tag{2.7}$$

$$\Theta_{SEP} = \arctan \frac{W_{w,SEP}}{U_{w,SEP}}. \tag{2.8}$$

Convergence is obtained once the residual value of the above parameters $\Delta_{TE}, \Delta_{SEP}, \Theta_{TE}, \Theta_{SEP}$ as well the total airfoil circulation, Γ_B , is lower than a chosen value, in this case set to 10^4.

Gerrard [14] has developed a vortex model to determine the oscillating variables of flow past a circular cylinder and found a reasonable agreement with experimental data. He

acknowledges that the essential characteristics of modeling flow separation is in the determination of rate of shedding of circulation at the boundary layer separation and the point of appearance of wake vortex carrying this shed circulation. Many authors [32] have successfully modeled wake oscillations behind a cylinder using different vortex modeling techniques.

Many of the features of complex flapping wings are accurately modeled with unsteady VLM and validated by experimental data, Fritz and Long [13]. They also found that the change in aerodynamics due to ignoring old part of the wake is minimal but the savings in CPU time is considerable, which gives insight into efficient wake modeling.

2.4 Research Objective

From literature survey, it is learned that when the flow separates over 2D LEI airfoil, flow becomes unsteady and formation to periodic vortex structures occur. Hence a unsteady model that can capture the time dependent forces on the airfoil is required. Hence, the focus of this study is directed towards developing unsteady inviscid model.

The various inviscid models reviewed have used different types of singularity elements 3.2.5 such as discrete vortices and distribution of vorticity elements.

The present study investigates various vortex panel techniques and attempts to formulate a aerodynamic model that is suitable for 2D LEI kite. The aimed outcome of the research is to have a model that is

- able to calculate aerodynamic forces (pressure distribution) generated on a 2D LEI kite airfoil
- also applicable within the typical kite flight domain which mainly includes
  - separated flow at most angle of attacks on the pressure side and at high angles of attack on the suction side [9]
- suitable for iterative design purposes. This means that the model should be capable enough to solve for aerodynamic forces iteratively for new kite geometries (since the kite is flexible) and this should not require any prior knowledge of the aerodynamic force distributions on the profile, as Breukels [6] used weight functions as an empirical input which is known priory
- able to overcome the limitations of modeling reattachment in the case of thickness free surfaces like membrane-wing kites and the requirement of high body-wake resolution in order to avoid flow protrude the surface [25]

The chord based Reynolds number of the flow over kite is of the order of 1-10 million, as discussed in the later section 3.1.1. Since for high Reynolds number flows, the viscous effects are confined to thin boundary layer on the airfoil and thin shear layers in the wake, the flow outside these regions can be assumed to be inviscid. The mathematical equations that govern such flows (inviscid flow theory) and further assumptions that lead to simplified flow theory referred as potential flow theory are discussed in chapter 3.

Boundary layer effects are not considered in the modeling objectives but a time dependent potential flow method along with viscous corrections[34] or inclusion of boundary layer calculations is possible [1] and would suffice the purpose of FSI analysis. But this implies that in order to model flow separation, location of flow separation on both sides of the airfoil of interest should be known in priory. And hence seems to be contradictory to our design objective but is feasible to overcome when the viscous corrections are included.

The suitability of vortex methods for kite FSI problem has already been justified by Rachel [25]. Since in the current study, 2D kite profiles are the subject of interest, the applicability of various vortex methods for modeling is discussed here. It is learned that discrete vortex methods as well as continuous distribution of vorticity methods can be used for modeling flow separation phenomenon. Discrete vortex elements are relatively easy to implement compared to distribution of vorticity over the panels. In the later, rotation of coordinate system to the local panel coordinates while estimating its influence and rotating back to global coordinates is an additional computation step to be considered.

Chapter 3

Theory of Inviscid, Incompressible and Irrotational Flow

The mathematical equations which govern the motion of fluid particles and variation of its properties are a set of differential equations which are derived from fundamental conservation laws of physics. This section presents the basics of fluid dynamics equations that govern the flows of particular interest (inviscid, incompressible and irrotational) for which potential flow theory is applicable. The conservation of mass and momentum equations are briefly explained and these equations are simplified using the above mentioned assumptions. The theory related to the current study is mostly based on the works of J. Katz & A. Plotkin obtained from the book *Low-Speed Aerodynamics* [23].

3.1 Governing Equations

The integral form of conservation laws of mass, momentum describing the fluid motion can be written using the concept of control volume. Consider a control volume in the fluid, shown in figure 3.1. The change in fluid properties such as density, momentum, etc., with respect to time in the control volume is the accumulation of the change of particular property over the control volume and the transfer of fluid property out and into control volume through the boundaries (control surface).

Conservation of Mass

Using divergence theorem, the differential form of conservation of mass which holds for any arbitrary control volume in the fluid is given by

$$\frac{\partial \rho}{\partial t} + \nabla \cdot \rho \mathbf{V} = 0. \tag{3.1}$$

The above equation is called continuity equation. And assuming incompressible flow, the continuity equation 3.1 reduces to

$$\nabla \cdot \mathbf{V} = 0 \tag{3.2}$$

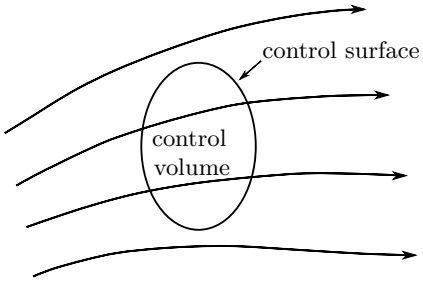

Figure 3.1: Arbitrary control volume in a fluid, modified from [23]

Conservation of Momentum

Following a similar approach used to derive conservation of mass 3.1, the rate of change in the momentum of the fluid flowing through the control volume is the sum of the accumulation of momentum per unit volume and the momentum flux across the control surface. The differential form of the conservation of momentum is given by

$$\frac{\partial \rho V_i}{\partial t} + \nabla \cdot \rho V_i \mathbf{V} - \rho f_i - \frac{\partial \tau_{ij}}{\partial x_j} = 0. \tag{3.3}$$

Newtonian fluid is defined as the fluid inside which the viscous stresses in the flow are in linear relation to the local strain rate (rate of change of deformation), i.e. the surface forces arising between the fluid elements are linearly related to the velocity derivatives as given by the well established relation

$$\tau_{ij} = -(p + \frac{2}{3}\mu \frac{\partial V_k}{\partial x_k})\delta_{ij} + \mu(\frac{\partial V_i}{\partial x_j} + \frac{\partial V_j}{\partial x_i}),$$

where μ is the viscosity coefficient, p is the pressure and δ_{ij} is the Kronecker delta function defined by

$$\delta_{ij} = \begin{cases} 1 & \text{if } i = j, \\ 0 & \text{if } i \neq j. \end{cases} \tag{3.4}$$

Substituting this into equation 3.3 and assuming incompressible flow simplifying using continuity equation 3.1, we obtain reduced form of Navier-Stokes equation

$$\rho[\frac{\partial \mathbf{V}}{\partial t} + \mathbf{V} \cdot \nabla \mathbf{V}] = \rho \mathbf{f} - \nabla p + \mu \nabla^2 \mathbf{V}. \tag{3.5}$$

3.1.1 Euler Equation

A high Reynolds number and low speed flow over an airfoil is characterized by thin boundary layers in which viscous effects are confined and fluid outside these boundary layers can be assumed to inviscid. And solution for inviscid flow in tis region would accurately predict pressure distribution and In a low speed flow (subsonic), the fluid density remains relatively constant however for higher speeds, some of the energy of the associated with object is utilized in compressing the fluid and locally changing the density. Typical chord based Reynolds number of the flow over a kite ranges between a minimum

of $3.33 \cdot 10^6$ for an altitude of $1000m$, apparent velocity $20\frac{m}{s}$ and a maximum of $8.10 \cdot 10^6$ art sea level and $45\frac{m}{s}$ apparent velocity, [25]. The Mach number of typical flow is low ($M \approx \frac{V_{apparent}}{C(=330\frac{m}{s})} \approx \frac{45}{330} \leq 0.14$). Hence the flow outside the boundary layers (external flow) can be assumed to be incompressible, $\rho = constant$, and inviscid, $\mu = 0$. With the inviscid flow assumption, Navier-Stokes relation 3.5 further simplifies to the so called Euler equation.

$$\frac{\partial \mathbf{V}}{\partial t} + \mathbf{V} \cdot \nabla \mathbf{V} = \mathbf{f} - \frac{\nabla p}{\rho}. \tag{3.6}$$

3.1.2 Vorticity and Circulation

The angular velocity of the fluid element about an axis perpendicular to the plane of paper (consider as z-axis and x, y axes in the plane of interest) is given by

$$\omega_z = \frac{1}{2}(\frac{\partial v}{\partial x} - \frac{\partial u}{\partial y})$$

Similarly considering in xz and yz plane will give 3D element's angular velocity about all the three axis as

$$\omega = \omega_x \mathbf{i} + \omega_y \mathbf{j} + \omega_z \mathbf{k},$$
$$\omega = \frac{1}{2}(\frac{\partial w}{\partial y} - \frac{\partial v}{\partial z})\mathbf{i} + \frac{1}{2}(\frac{\partial u}{\partial z} - \frac{\partial w}{\partial x})\mathbf{j} + \frac{1}{2}(\frac{\partial v}{\partial x} - \frac{\partial u}{\partial y})\mathbf{k},$$
$$\omega = \frac{1}{2}(\nabla \times \mathbf{V}).$$

The vorticity (ζ) is defined as twice of angular velocity. The appearance of 2ω is more frequent and just for the sake of numerical convenience, vorticity is defined as

$$\zeta = 2\omega = (\frac{\partial w}{\partial y} - \frac{\partial v}{\partial z})\mathbf{i} + (\frac{\partial u}{\partial z} - \frac{\partial w}{\partial x})\mathbf{j} + (\frac{\partial v}{\partial x} - \frac{\partial u}{\partial y})\mathbf{k} = \nabla \times \mathbf{V}. \tag{3.7}$$

Stokes's theorem relates the surface integral of curl of vector field to the line integral of the vector field over its boundary. Using Stokes's theorem, the vorticity on the surface S can be related to line integral along the boundary of the surface C as,

$$\int_S (\nabla \times \mathbf{V}) \cdot \mathbf{n} dS = \int_S \zeta \cdot \mathbf{n} dS = \oint_C \mathbf{V} \cdot \mathbf{dl}$$

The line integral on the right had side is defined as circulation denoted by Γ. Circulation is related to vorticity as

$$\Gamma = \oint_C \mathbf{V} \cdot \mathbf{dl} = \int_S \zeta \cdot \mathbf{n} dS. \tag{3.8}$$

When the flow is irrotational ($\nabla \times \mathbf{V} = 0$), then circulation is also zero according to equation 3.8.

In order to derive the equation that governs the change in vorticity of fluid elements in a flow, take curl of Navier-Stokes equation 3.5. and further simplifying assuming the flow

to be incompressible and various other vector operations, we arrive at

$$\frac{\partial \zeta}{\partial t} + \mathbf{V} \cdot \nabla \zeta = \nabla \times \mathbf{f} + \nu \nabla^2 \zeta,$$
$$\frac{D\zeta}{Dt} = \nabla \times \mathbf{f} + \nu \nabla^2 \zeta. \tag{3.9}$$

If the flow is assumed to be inviscid, then the equation becomes

$$\frac{D\zeta}{Dt} = \nabla \times \mathbf{f} \tag{3.10}$$

The equation 3.10 implies that vorticity is generated in a inviscid flow by the change in force field. Hence for two dimensional incompressible and inviscid flow, vorticity can only be generated by the curl of force field. Since the force field is created on the solid boundary, the flow is to be considered rotational at the boundary.

Considering only the outer region (region outside the boundary layer), we know that body forces in this region are conservative ($\nabla \times \mathbf{f} = 0$) and for higher Reynolds number flows (coefficient of viscosity is low), it can be inferred from equation 3.9 that the vorticity created in the outer flow region is negligible. Hence the flow in the outer region (excluding the wake region) can be considered to be irrotational.

3.2 Potential Flow Theory

For high Reynolds number flow, we established that the vorticity generated outside the boundary layer is negligible (from equation 3.9), since the viscous effects are insignificant in this region. From the assumptions that the flow to be irrotational and inviscid, the flow in the outer region is free of vorticity generation, we have

$$\nabla \times \mathbf{V} = 0.$$

3.2.1 Velocity Potential

We know from the vector identity that curl of gradient of scalar function is always zero ($\nabla \times \nabla A = 0$). So there exists a scalar potential function ϕ, whose gradient is equal to the velocity vector such that mathematically irrotationality condition is always satisfied. Hence for irrotational flow, we define a velocity potential ϕ such that its gradient is equal to velocity field,

$$\mathbf{V} = \nabla \phi. \tag{3.11}$$

The velocity components u, v, w in cartesian coordinates is given by

$$u = \frac{\partial \phi}{\partial x}, v = \frac{\partial \phi}{\partial y}, w = \frac{\partial \phi}{\partial z}. \tag{3.12}$$

Assuming the flow to be incompressible and substituting velocity potential into the continuity equation 3.2, we arrive at Laplace equation

$$\nabla \cdot \mathbf{V} = \nabla \cdot \nabla \phi = \nabla^2 \phi = 0. \tag{3.13}$$

In summary, the velocity field of an inviscid incompressible and irrotational flow can be obtained from a scalar velocity potential which is solution of Laplace's equation. Once the velocity field is determined, Euler equation 3.6 determines the pressure distribution.

Since the Laplace equation is second-order, linear, differential equation, the solutions of Laplace equation are linear. If a flow field is represented by elementary solutions $\phi_1, \phi_2, \phi_3, ..., \phi_n$ which are solutions of Laplace equation, then the total velocity potential of that region can be estimated as superposition of all the individual potentials. And the resultant velocity field is given by the superposition of velocity due to individual velocity potentials, as given by

$$\phi = \phi_1 + \phi_2 + \phi_3 + ... + \phi_n,$$
$$\mathbf{V} = \mathbf{V}_1 + \mathbf{V}_2 + \mathbf{V}_3 + ... + \mathbf{V}_n.$$

This property of superposition of Laplace equation paves way for modeling flow field around complex boundaries using combination of elementary solutions.

3.2.2 Bernoulli's Equation

Euler equation 3.6 expanded using the vector identity

$$\mathbf{V} \cdot \nabla \mathbf{V} = \nabla \frac{V^2}{2} - \mathbf{V} \times (\nabla \times \mathbf{V})$$

and incorporating irrationality assumption $\nabla \times \mathbf{V} = 0$, we get

$$\frac{\partial \mathbf{V}}{\partial t} + \nabla \frac{V^2}{2} = \mathbf{f} - \nabla \frac{p}{\rho}. \tag{3.14}$$

Rewriting velocity in terms of velocity potential, the above equation becomes

$$\nabla \frac{\partial \phi}{\partial t} + \nabla \frac{V^2}{2} = \mathbf{f} - \nabla \frac{p}{\rho}.$$

Assuming the body force acting on the fluid are conservative, then it can be expressed in terms of a potential function as $\mathbf{f} = -\nabla E$. If the body force acting is gravity then the potential function is given by $E = gZ$, where g is acceleration due to gravity and Z is the distance measured along the vertical axis. Substituting this form of $\mathbf{f}$, the above equation becomes

$$\nabla (E + \frac{p}{\rho} + \frac{V^2}{2} + \frac{\partial \phi}{\partial t}) = 0,$$

$$E + \frac{p}{\rho} + \frac{V^2}{2} + \frac{\partial \phi}{\partial t} = C(t), \tag{3.15}$$

where C(t) is dependent only on time and is constant over the entire space of flow field. For incompressible inviscid, irrotational flow and steady flow, using Bernoulli equation 3.15 pressure and velocity can be compared between at any two points in a potential flow. However if the flow is rotational, the constant on the right hand side is different for different streamlines. Hence comparison of pressure and velocity can be made between points only along the streamline of interest. Since right hand side is constant over space,

a more insightful form of Bernoulli equation is derived when it is applied for two different points in fluid. Considering one of the points to be reference point at infinity, and the other point to be arbitrary, the equation becomes

$$E + \frac{p}{\rho} + \frac{V^2}{2} + \frac{\partial \phi}{\partial t} = [E + \frac{p}{\rho} + \frac{V^2}{2} + \frac{\partial \phi}{\partial t}]|_\infty$$

As reference point is by assumption located far field such that it is free from disturbances induced, we can neglect the rate of change of potential and also difference in body forces is negligible, $E_\infty = E$, we obtain

$$p - p_\infty = \rho[\frac{V_\infty^2}{2} - \frac{V^2}{2} - \frac{\partial \phi}{\partial t}]. \tag{3.16}$$

Dividing by free stream dynamic pressure $\frac{1}{2}\rho V_\infty^2$, we obtain pressure coefficient $C_p = \frac{p - p_\infty}{\frac{1}{2}\rho V_\infty^2}$ on the left hand side and the equation becomes

$$C_p = \frac{p - p_\infty}{\frac{1}{2}\rho V_\infty^2} = 1 - \frac{V^2}{V_\infty^2} - \frac{2}{V_\infty^2}\frac{\partial \phi}{\partial t}. \tag{3.17}$$

Now assuming the flow to be steady, the rate of change of potential becomes zero and the Bernoulli equation reduces to

$$C_p = \frac{p - p_\infty}{\frac{1}{2}\rho V_\infty^2} = 1 - \frac{V^2}{V_\infty^2}. \tag{3.18}$$

Consider the case with flow separation over an airfoil as shown in figure 3.2. The flow field can be divided into two regions, separated flow region R_2 which is between the separated and trailing edge wakes and outer flow region R_1 (which is remaining region other than separated flow region in the flow field). Let h_1, h_2 be the total heads of the regions R_1, R_2 respectively. Assuming potential flow, irrotational every where except at the airfoil surface and along the wakes, applying Bernoulli equation at points in different regions will be equal to corresponding total head values as

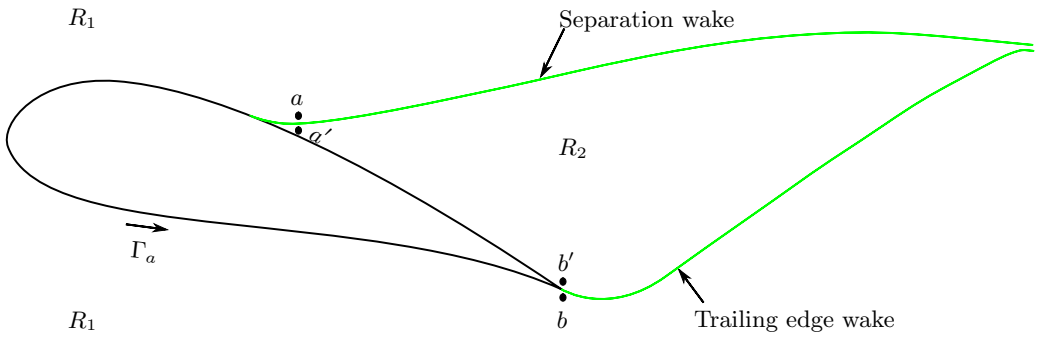

Figure 3.2: Separation region over the airfoil indicated by R_2.

$$p_a + \frac{1}{2}V_a^2 + \frac{\partial \phi_a}{\partial t} = h_1,$$
$$p_{a'} + \frac{1}{2}V_{a'}^2 + \frac{\partial \phi_{a'}}{\partial t} = h_2. \tag{3.19}$$

Hence while calculating the pressure coefficient in region R_2 using unsteady Bernoulli equation, the jump in the total head ($\Delta h = h_2 - h_1$) should also be considered. In region R_2 the coefficient of pressure becomes

$$C_p = \frac{p - p_\infty}{\frac{1}{2}\rho V_\infty^2} = 1 - \frac{V^2}{V_\infty^2} - \frac{2}{V_\infty^2}\frac{\partial \phi}{\partial t} - \frac{2}{V_\infty^2}\Delta h. \tag{3.20}$$

3.2.3 Estimation of aerodynamic loads and coefficients

Depending on the singularity elements used for modeling, the distribution of circulation (or vortex distribution) is obtained as a solution. Using the corresponding Bernoulli's equation, pressure distribution on the airfoil can be estimated. The force acting on each panel (considering the discretization of airfoil in to several panels) can be calculated from the pressure and total aerodynamic loads can be obtained by summing the corresponding force components. This approach is, in general, applicable to any type of vortex model but not so straight forward because obtained circulation (vortex distribution) should be post processed using Bernoulli's equation for obtaining loads. The lift and drag coefficients obtained from the pressure coefficient is given by

$$C_L = \sum_{i=1}^{i=N_{pan}} C_{P_i} \cos \alpha_i,$$
$$C_D = \sum_{i=1}^{i=N_{pan}} C_{P_i} \sin \alpha_i, \tag{3.21}$$

where α_i is the inclination of i^{th} panel with respect to x-axis, as shown in figure 3.3 and N_{pan} is total number of panels. A much more straight forward way to estimate lift is by using Kutta-Joukowski theorem which states

$$\mathbf{F} = \rho \mathbf{V}_\infty \times \mathbf{\Gamma}, \tag{3.22}$$

where $\mathbf{F}$ is resultant aerodynamic force per unit width in an incompressible, inviscid and irrotational flow and the direction Γ is given by right hand rule (if clockwise orientated then circulation is directed into the plane). In the case of two dimensional flow, resultant aerodynamic force obtained by using equation 3.22 must be perpendicular to free stream, and hence resultant aerodynamic force is lift force ($L = \rho V_\infty \Gamma$). The resultant pressure acting at the i^{th} panel is given by lift per unit length, using Kutta-Joukowski theorem which becomes

$$\Delta p_i = \rho V_\infty \frac{\Gamma_i}{\Delta l_i} = \rho V_\infty \gamma_i.$$

The drag force estimated by potential flows should be zero because viscosity is not considered in potential flow theory. The drag coefficient C_D for a cylinder using potential theory is found to be zero. This is referred as D'Alembert's paradox [23].

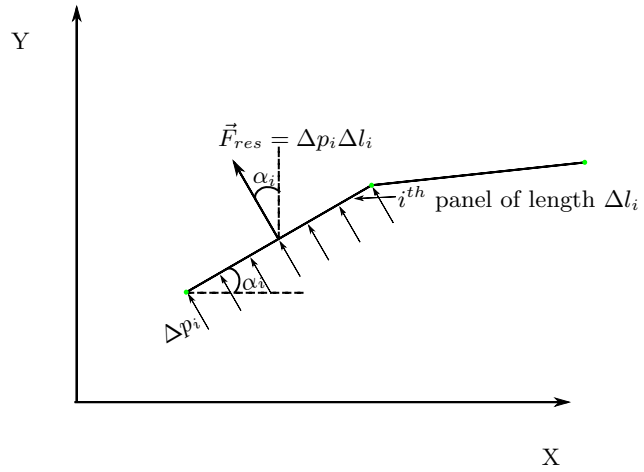

Figure 3.3: Resultant force acting on i^{th} panel due to pressure at the panel ΔP and α_i is the orientation of the panel

3.2.4 Boundary Conditions

Applying correct boundary conditions while solving the Laplace equation is vital, since the physics of flow is interpreted in the mathematical domain only through the boundary conditions inputs. The typical boundary conditions for flow over solid surface is the requirement that on a stationary solid boundary both the normal and tangential velocity components are zero. But the potential flow equations are discussed in previous sections are applicable only in inviscid outer flow region. The tangential velocity components are zero in the thin boundary layer region and hence these conditions are not applied as a part of potential flow solution.
The boundary conditions considered are no flow penetration through the solid surface, i.e. zero normal velocity components,

$$\frac{\partial \phi}{\partial n} = 0. \tag{3.23}$$

In addition to this, the far field condition forcing induced disturbances to decay to zero which can be interpreted as the potential due to the body must become negligible in the far field ($r \to \infty$),

$$\lim_{r \to \infty} \phi_{body} = 0. \tag{3.24}$$

The velocity profile obtained as a solution of the Laplace equation depict the velocities in the outer flow region.

3.2.5 Singularity Elements

In this section, the elementary solutions of Laplace equation, which form the basis of the models that are developed in this thesis are introduced. These elementary solutions are built such that they automatically satisfy one of the required boundary condition, that velocity fields (or potential) due to the elements decay as $r \to \infty$. Also it is noted that as $r = 0$, the velocity becomes singular ($\|\mathbf{V}\| \to \infty$), hence the basic elements are called singular elements.

The singularity element that is used in the present study is point vortex element. There are many other elements such as point source, constant-strength and linearly varying source, vortex distribution elements available in the literature and the reader is referred to [23] for more details. Here only one of each kind of singularity such as discrete (point), constant strength, linear strength elements are introduced.

Point vortex element

Point singularity elements are the most simple and are computationally efficient elements. The potential ϕ at a point $P(x, y)$due to a point vortex with strength Γ located at point P_0 (x_0, y_0) is given by,

$$\phi = -\frac{\Gamma}{2\pi} \tan^{-1} \frac{y - y_0}{x - x_0}. \tag{3.25}$$

The velocity induced can be estimated by using equation 3.12 as,

$$u = \frac{\Gamma}{2\pi} \frac{y - y_0}{(x - x_0)^2 + (y - y_0)^2}, \tag{3.26}$$

$$v = \frac{\Gamma}{2\pi} \frac{y - y_0}{(x - x_0)^2 + (y - y_0)^2}. \tag{3.27}$$

The point elements are discrete and when a surface is modeled, it is clear that they cannot represent a continuous surface. A more refined representation of surface can be achieved with continuous distribution of singularity elements which can be obtained by dividing surface into panels. Such continuous distribution of singularity elements are discussed below.

Constant strength source element

We define source strength density, i.e. constant strength per unit length σ and assumed it is distributed along x axis. The influence of such an element at a point $P(x, y)$ can be viewed as the summation of influence of discrete elements spanning along the length. The total influence can be obtained by integrating along the length as

$$\phi = \frac{\sigma}{2\pi} \int_{x_1}^{x_2} \ln \sqrt{(x - x_0) + (y^2)} dx_0,$$

$$= \frac{\sigma}{4\pi}[(x - x_1) \ln((x - x_1)^2 + y^2) - (x - x_2) \ln((x - x_2)^2 + y^2) + 2y(\tan^{-1} \frac{y}{x - x_2} - \tan^{-1} \frac{y}{x - x_1})]. \tag{3.28}$$

And the corresponding induced velocity components are given by,

$$u = \frac{\sigma}{4\pi} \ln \frac{(x - x_1)^2 + y^2}{(x - x_2)^2 + y^2}, \tag{3.29}$$

$$v = \frac{\sigma}{4\pi}[\tan^{-1} \frac{y}{x - x_2} - \tan^{-1} \frac{y}{x - x_1}]. \tag{3.30}$$

This kind of continuous distribution of singularity elements over the panels using constant strength elements results in discontinuity at the panel edges.

Linear strength vortex element

A linear distribution of singularity, using the principle of superposition, can be decomposed into constant strength and linearly varying element. For simplicity only the linearly varying element is dealt and these results can be added to constant strength elements to arrive at equivalent result of total element.

Assuming the element in placed along x axis such that linearly varying strength is defined by $\gamma(x) = \gamma_1 x (x_1 \leq \xi \leq x_2)$, where γ_1 is constant. The potential created at a point $P(x, y)$ is obtained again by a similar integration as discussed for constant strength element

$$\phi = -\frac{\gamma_1}{2\pi} \int_{x_1}^{x_2} x_0 \tan^{-1} \frac{y}{x - x_0} dx_0,$$
$$= -\frac{\gamma_1}{2\pi} [\frac{xy}{2} \ln \frac{r_1^2}{r_2^2} + \frac{y}{2}(x_1 - x_2) + \frac{x^2 - x_1^2 - y^2}{2}\theta_1 - \frac{x^2 - x_2^2 - y^2}{2}\theta_2], \tag{3.31}$$

where $\theta_1 = \tan^{-1} \frac{y}{x - x_1}, \theta_2 = \tan^{-1} \frac{y}{x - x_2}$. The linearly varying strength varies from γ_j to γ_{j+1} in the interval $(x_j \leq x \leq x_{j+1})$ such that

$$\gamma(x) = \gamma_j + \gamma_{j+1}(x - x_1), \quad \text{for} \quad x_1 \leq x \leq x_2$$

Adding the velocity components due to constant strength element and generalizing the equation in terms of γ_j, γ_{j+1}, so it becomes easy to interpret while coding the influence terms of nodal strengths of such an element.

$$u = \frac{\gamma_j}{2\pi l}[-y \ln \frac{r_j}{r_{j+1}} + (x_{j+1} - x)(\theta_{j+1} - \theta_j)]$$
$$+ \frac{\gamma_{j+1}}{2\pi l}[y \ln \frac{r_{j+1}}{r_j} + (x - x_j)(\theta_{j+1} - \theta_j)], \tag{3.32}$$
$$v = \frac{\gamma_j}{2\pi l}[(x_{j+1} - x) \ln \frac{r_{j+1}}{r_j} - (x_{j+1} - x) - y(\theta_{j+1} - \theta_j)]$$
$$+ \frac{\gamma_{j+1}}{2\pi l}[(x - x_j) \ln \frac{r_{j+1}}{r_j} + (x_{j+1} - x_j) + y(\theta_{j+1} - \theta_j)], \tag{3.33}$$

where l is the length of the element (panel).

Similarly, linear strength source influence terms can be derived. Also there are high order singularity elements (quadratic, cubic etc.) available, for further details the reader is referred to [23].

3.2.6 Simplification of Bernoulli equation

Now the equations that relate vorticity distribution to the velocity around the distribution are derived. Consider a vortex distribution $\gamma(x)$ in the interval $x_1 \leq x \leq x_2$ along x-axis, as shown in figure 3.4. The tangential velocities $u(x, z = \pm 0)$ just above and below along the vortex distribution is given by

$$u(x, \pm 0) = \frac{\partial \phi}{\partial x}(x, \pm 0) = \pm \frac{\gamma(x)}{2},$$
$$u(x, 0+) - u(x, 0-) = \frac{\partial \phi}{\partial x}(x, 0+) - \frac{\partial \phi}{\partial x}(x, 0-) = \gamma(x). \tag{3.34}$$

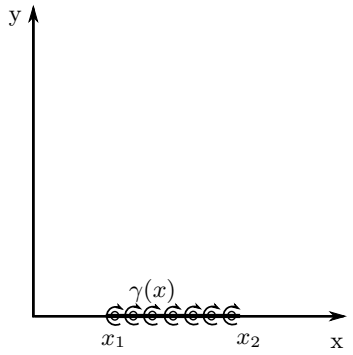

Figure 3.4: Distribution of vorticity.

This equation can be derived using the definition of velocity induced by vortex distribution at a point (x, z), as given in third chapter of [23]. The potential jump across the vortex distribution, using the definition of potential 3.12 is given by

$$\phi(x, 0+) - \phi(x, 0-) = \int_{x_1}^{x} \frac{\gamma(x)}{2} dx - \int_{x_1}^{x} -\frac{\gamma(x)}{2} dx,$$
$$\Delta\phi(x) = \Gamma(x). \tag{3.35}$$

here potential ahead of vortex distribution is assumed to be zero and $\Gamma(x)$ is the circulation around the path surrounding the segment x_1 to x.

Consider a flow field with uniform free stream in x direction with a combination of singularity elements of potential $\phi = \phi_1 + \phi_2 + ... + \phi_n$. The velocity at a point (x,y) is given by

$$\mathbf{V} = \mathbf{V}_\infty + \nabla\phi(x, y) = (V_\infty \cos\alpha + \frac{\partial\phi}{\partial x})\mathbf{i} + (V_\infty \sin\alpha + \frac{\partial\phi}{\partial y})\mathbf{j}.$$

Substituting this into steady state Bernoulli equation 3.18, and considering small disturbance flow assumptions [23], we get,

$$p - p_\infty = \rho V_\infty \frac{\partial\phi}{\partial x}$$

Applying this to estimate resultant pressure acting at i^{th} panel and using equation 3.34 we get

$$\Delta p_i = \rho V_\infty \gamma_i, \tag{3.36}$$

where γ_i is the circulation per unit strength present on i^{th} panel.

In unsteady flows, additional contribution of fluid acceleration $\frac{\partial\phi}{\partial t}$ which is an outcome from unsteady Bernoulli equation 3.17, must be considered and the resultant pressure acting at i^{th} panel is given by

$$\Delta p_i = 2\rho(V_\infty \frac{\gamma_i}{2} + \frac{\partial\phi_i}{\partial t}), \tag{3.37}$$

In order to validate the unsteady lift due to impulsively started flat plate, the indicial response function $\Phi(\tau)$, which is the ratio of unsteady lift (excluding the fluid acceleration)

and corresponding steady state value is used. The is determined by Wagner function whose two term approximation is given by [5]

$$\Phi(\tau) = 1 - 0.165e^{-0.045\tau} - 0.335e^{-0.3\tau}, \tag{3.38}$$

where $\tau = \frac{V_\infty t}{\frac{c}{2}}$ is the distance traveled by flat plate in terms of half-chord length.

3.3 Kutta condition

In order to obtain a unique solution corresponding to flow over the airfoil, Kutta condition needs to be employed along with the other boundary conditions. The mathematical formulation of Kutta condition varies according to the model used. In the case of steady attached flow conditions, applying the steady Bernoulli's equation 3.18 at points A and B present on either side of the trailing edge, as shown in figure 3.6, we get

$$\frac{V_A^2 - V_B^2}{2} = \frac{p_B - p_A}{2}.$$

There exists zero loading at the trailing edge of the airfoil and this results in equal velocities at the trailing edge panels. This also can be interpreted as no vorticity shedding in the steady case from trailing edge since the velocities are equal on either side of the trailing edge.

$$V_A = V_B.$$

An approximate expression relating rate of circulation shed [22] and velocities around

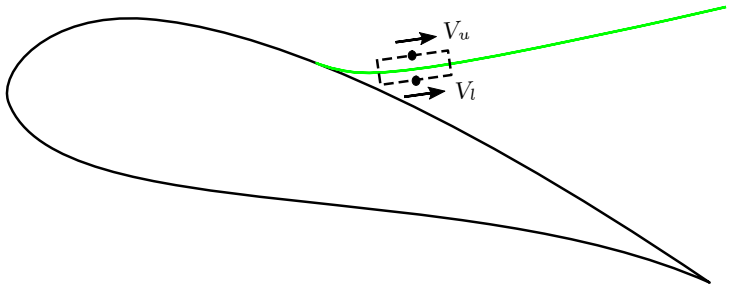

Figure 3.5: Estimation of circulation shed in terms of velocity using the line integral of velocity definition.

the portion enclosing circulation is given by time derivative of line integral of velocity around the portion shown in figure 3.5

$$\frac{d\Gamma}{dt} = \frac{d}{dt}\oint V ds = \frac{d(V_u ds - V_l ds)}{dt} \approx \frac{1}{2}(V_u^2 - V_l^2). \tag{3.39}$$

The condition that line integral of velocity along the perpendicular line segments is taken as zero because there wont be any cross flow along the wake element. This can be

interpreted as vorticity shed into the flow which creates a discontinuity in velocity profile (shear layer) and as wake elements convect in the region shear layer develops accordingly. The above derived relations 3.34, 3.35, 3.39 are used to modify the Kutta condition for different flow conditions and understand the relation between shed circulation and circulation developed on the airfoil as discussed in next section.

However for unsteady attached flows, the formulation of Kutta condition changes. Applying unsteady Bernoulli's equation at the trailing in a similar manner as discussed above, we get

$$\frac{\partial \phi_A}{\partial t} - \frac{\partial \phi_B}{\partial t} + \frac{V_A^2 - V_B^2}{2} = \frac{p_B - p_A}{2}.$$

Using again the physical justification that zero loading exists at the trailing edge i.e.

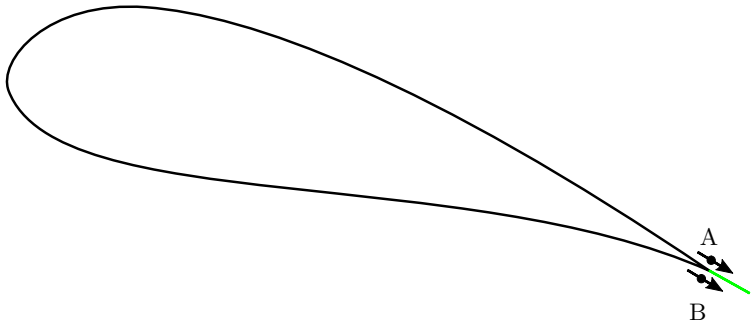

Figure 3.6: Attached flow over the airfoil.

$p_A = p_B$, the above equation becomes

$$\begin{aligned} \frac{\partial \phi_B}{\partial t} - \frac{\partial \phi_A}{\partial t} &= \frac{V_A^2 - V_B^2}{2}, \\ -\frac{\partial \Delta\phi_{TE}}{\partial t} &= \frac{\partial \Gamma_{TE}}{\partial t}, \\ -\frac{\partial \Gamma_a}{\partial t} &= \frac{\partial \Gamma_{TE}}{\partial t}. \end{aligned} \tag{3.40}$$

The left hand side of the above equation represents the rate of change of circulation on the airfoil ($-\frac{\partial \Gamma_a}{\partial t}$), as explained above 3.35. Here the right hand side represents the vorticity being shed from the trailing edge ($\frac{\partial \Gamma_{TE}}{\partial t}$), as explained above 3.39, as shown in figure 3.6. The above equation is another approach to Kelvin's theorem which is discussed in section 3.4 below.

In the case of flow separation on the airfoil, unsteady Kutta condition takes a different form. Consider the separated flow as shown in figure 3.2, the total head jump given by applying Bernoulli equation across the separation point is

$$\Delta h = h_2 - h_1 = [p_{a'} + \frac{1}{2}V_{a'}^2 + \frac{\partial \phi_{a'}}{\partial t}] - [p_a + \frac{1}{2}V_a^2 + \frac{\partial \phi_a}{\partial t}].$$

We know that $p_a = p_{a'}$ because of zero loading on the separation wake element. The above equation becomes

$$\Delta h = \frac{1}{2}(V_{a'}^2 - V_a^2) + \frac{\partial(\phi_{a'} - \phi_a)}{\partial t}. \tag{3.41}$$

Similarly head jump calculated across the trailing edge is given by

$$-\Delta h = \frac{1}{2}(V_b^2 - V_{b'}^2) + \frac{\partial(\phi_b - \phi_{b'})}{\partial t}. \tag{3.42}$$

Equating the head jumps calculated at both the wakes and rearranging the terms, we get

$$\begin{aligned} \frac{\partial(\phi_{a'} - \phi_a)}{\partial t} + \frac{\partial(\phi_b - \phi_{b'})}{\partial t} &= \frac{1}{2}(V_b^2 - V_{b'}^2) + \frac{1}{2}(V_{a'}^2 - V_a^2), \\ \frac{\partial \Gamma_a}{\partial t} &= -[\frac{\partial \Gamma_{SP}}{\partial t} + \frac{\partial \Gamma_{TE}}{\partial t}], \end{aligned} \tag{3.43}$$

where Γ_{SP}, Γ_{TE} are the circulation strengths of separation and trailing edge wakes re-

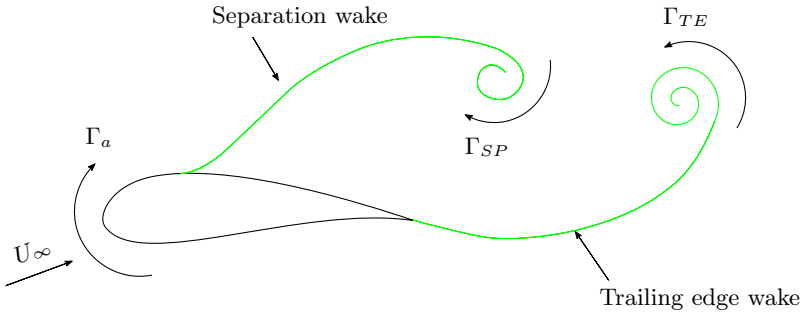

Figure 3.7: Separated flow over the airfoil.

spectively and Γ_a is the circulation strength of the airfoil, as shown in figure 3.7. It can be noticed that unsteady Kutta condition in both cases (attached flow and case with flow separation) governs that all the vorticity developed on the airfoil is being shed into the wake. In the case of attached flow, vorticity is shed only at the trailing edge and in the case with flow separation, vorticity is shed from both the locations i.e separation point and trailing edge. Also the jump in total head in the case of flow separation should be considered while evaluating pressure distribution in the separated flow region R_2, shown in figure 3.2, which is given in equation 3.20

3.4 Kelvin's Theorem

Consider an incompressible, inviscid flow with conservative body forces acting in the region, the time rate of circulation around a fluid curve C as shown in figure 3.8 is given

$$\frac{D\Gamma}{Dt} = \frac{D}{Dt}\oint_C \mathbf{V} \cdot \mathbf{dl} \tag{3.44}$$

$$= \oint \frac{D\mathbf{V}}{Dt} \cdot \mathbf{dl} + \oint_C \mathbf{V} \cdot \frac{D}{Dt}\mathbf{dl}, \tag{3.45}$$

where $\frac{D\mathbf{V}}{Dt} = \mathbf{a}$ and $\frac{D}{Dt}\mathbf{dl} = \mathbf{dV}$. Substituting these into the equation, we get

$$\frac{D\Gamma}{Dt} = \oint_C \mathbf{a} \cdot \mathbf{dl} + \oint_C \mathbf{V} \cdot \mathbf{dV},$$

and the closed integral of an exact differential term is zero $\oint_C \mathbf{V} \cdot \mathbf{dV} = \oint_C d(\frac{V^2}{2}) = 0$ and the acceleration from Euler equation 3.6 is given by

$$\mathbf{a} = -\nabla\frac{p}{\rho} + \mathbf{f}.$$

Substituting into rate of change of circulation equation, we get

$$\frac{D\Gamma}{Dt} = \oint_C d(\frac{p}{\rho}) + \oint_C \mathbf{f} \cdot \mathbf{dl} = 0. \tag{3.46}$$

First term on the left hand side is a an exact differential term and since the integration is carried over a closed loop, this term vanishes. The forces acting in the flow field are considered conservative, we know the work done by a conservative force around a closed path is zero. Kelvin's theorem states that the time rate of change of circulation around

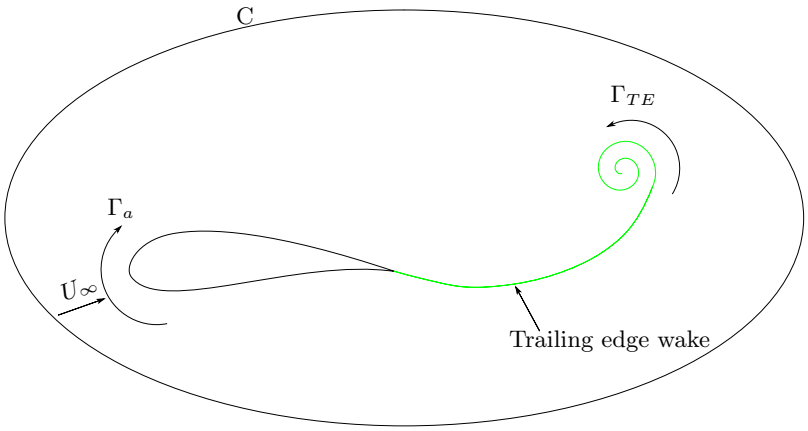

Figure 3.8: Separation region over the airfoil indicated by R_2.

a closed curve consisting of the same fluid elements is zero. This implies circulation is conserved in the entire region. Applying this to the airfoil with attached flow over it as shown in figure 3.8, we get

$$\frac{D\Gamma}{Dt} = \frac{D\Gamma_a}{Dt} + \frac{D\Gamma_{TE}}{Dt} = 0,$$

which is similar to the result in equation 3.40 achieved by the application of Bernoulli equation. Similarly application of Kelvin's theorem to the airfoil at certain angle of attacks when flow separation occurs, as shown in figure 3.7, gives

$$\frac{D\Gamma}{Dt} = \frac{D\Gamma_a}{Dt} + \frac{D\Gamma_{TE}}{Dt} + \frac{D\Gamma_{SP}}{Dt} = 0,$$

which is the similar result achieved in equation 3.43. However for 2D LEI kite profile, there is an additional separation wake emanating from the pressure surface near the leading edge as shown in figure 2.7. The equation 3.4 has to be modified for the 2D LEI kite airfoil.

3.5 Methodology of computational implementation

In order to arrive at the desired aerodynamic model, development of computational model begins with modeling steady state attached flow on a cambered plate and then to the corresponding unsteady models. The table 3.1 given below presents the step wise phase of models that are to be developed and validated to arrive at desired model with the capability of modeling two separation wakes and a trailing edge wake for 2D LEI kite airfoils.

Model	Description	Schematic representation
Steady state	Attached flow on a flat/cambered plate	
Unsteady single wake	Unsteady model to mimic attached flow on flat/cambered plate	
Unsteady double wake	Unsteady model to capture separation flow over flat/cambered plate	
Unsteady triple wake	Unsteady model to capture separation flow over 2D LEI kite airfoil	

Table 3.1: Schematic representation of step by step development phase of computational models.

Chapter 4

Computational Implementation

4.1 Introduction

In this section various steps involved in developing the required computational model is discussed. In the initial stage of the project, a steady state model is developed and this is extended to a unsteady model by the inclusion of time stepping and release of vorticity from prescribed locations. The computational model is aimed to capture two types of flows, one is fully attached flow over airfoils and the other, separated flow. In order to model fully attached flows, a single wake model is employed. In this model, vorticity is shed from trailing edge at each time step and is convected with the velocity experienced during that time step. The strength of the vorticity shed is governed by Kelvins theorem, equation 3.46. Single wake model overestimates the lift when applied to capture separated flows and is unable to model the physics of the separated flow accurately. Hence a double wake model is implemented in which vorticity is released from two locations trailing edge and at the location at which flow separates from the airfoil. For given inflow conditions, the flow separation location is supplied as an input to the double wake model obtained either RANS simulations or viscous calculations using XFOIL. Similarly, in order to capture flow over typical leading edge inflatable kite airfoils, a triple wake model is developed in which vorticity is released from three locations one being the trailing edge and other two are the potential flow separation locations on such airfoils. And the data of flow separation locations are again supplied to triple wake model. All the models are two dimensions and flow is assumed to be inviscid, incompressible.

This chapter will present the development wake models starting with the description of steady state model in section 4.2 and unsteady single wake model in section 4.3.

4.2 Steady state model

A flat plate is considered for validating the steady state model developed. The geometry is discretized to a set of N_{pan} panels of equal length. It is known that higher the N_{pan},

better the discretization of the airfoil, since it accurately represents the airfoil but the computational time is proportional to ${N_{pan}}^2$. This becomes considerable in the later part of the unsteady models because then the equations are solved at every time step which is not present in the steady state model. Hence a compromise has to be made between the computational time and accuracy of the results. The flat plate geometry is divided into

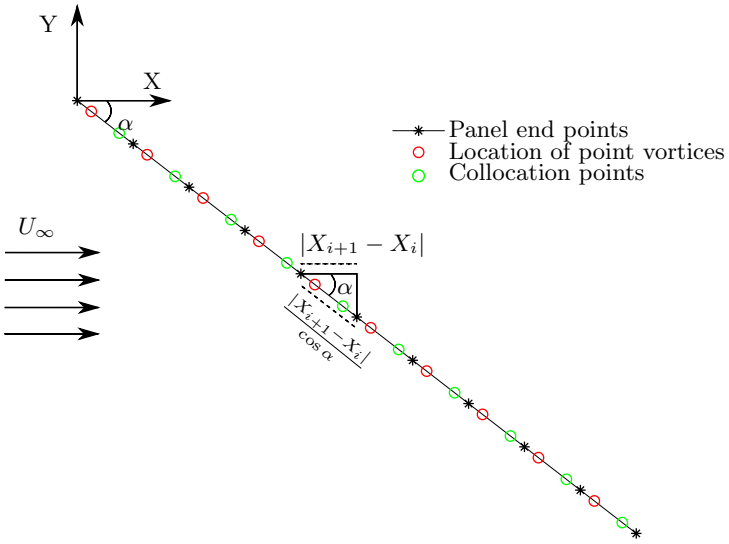

Figure 4.1: Flat plate at angle of attack α is discretized into several panels, point vortex singularity elements located at quarter chord and collocation points at three-quarter chord locations on each panel.

N_{pan} straight panels, as a result there will be $N_{pan}+1$ panel nodes, one at the end of each panel. A point vortex of unknown circulation strength is placed at quarter chord point of each panel which represents the vorticity generated on that panel. Collocation point is defined to be three quarter chord point as shown in figure 4.1, and at this point the non penetration boundary condition is enforced. The construction of the influence matrix and the resultant system of equations is discussed in section 4.2.1. The computation of resultant aerodynamic pressure and loads is presented in section 4.2.2.

4.2.1 Formation of system of equations

In the steady state model, the number of unknowns are N_{pan} i.e. $\Gamma_1, \Gamma_2, \Gamma_3, ..., \Gamma_N$, strength of point vortices, one on each panel. The boundary conditions available are N_{pan} non flow penetration conditions employed at each collocation point. This implies the normal flow component at each collocation point must be zero which results in the

following system of linear equations

$$\begin{bmatrix} C_{11} & \dots & C_{1j} & \dots & C_{1N_{pan}} \\ \vdots & \ddots & \vdots & \ddots & \vdots \\ C_{i1} & \dots & C_{ij} & \dots & C_{iN_{pan}} \\ \vdots & \ddots & \vdots & \ddots & \vdots \\ C_{N_{pan}1} & \dots & C_{N_{pan}j} & \dots & C_{N_{pan}N_{pan}} \end{bmatrix} \begin{bmatrix} \Gamma_1 \\ \vdots \\ \Gamma_i \\ \vdots \\ \Gamma_{N_{pan}} \end{bmatrix} = \begin{bmatrix} RHS_1 \\ \vdots \\ RHS_i \\ \vdots \\ RHS_{N_{pan}} \end{bmatrix}$$

Here the matrix C is defined as the influence matrix whose terms contain the normal component of velocity due to each point vortex at particular collocation point. The normal component of velocity induced by j^{th} point vortex at i^{th} collocation point is given by

$$C_{i,j} = [U_{i,j}V_{i,j}] \cdot \mathbf{n_i}, \tag{4.1}$$

where $[U_{i,j}V_{i,j}]$ is the velocity induced by point vortex given by equation 3.27 and $\mathbf{n_i}$ is the normal vector of i^{th} panel.

The matrix on the right hand side consists known normal component of velocities at the collocation points. Here in this case the normal component of velocity due to free stream is considered with an opposite sign so that when it adds to zero normal velocity at each collocation point. N_{pan} rows in the above matrix correspond to N_{pan} non flow penetration boundary conditions.

$$RHS_i = -\mathbf{U}_\infty \cdot \mathbf{n_i} \tag{4.2}$$

Here, in the case of flat plate, a additional Kutta condition to establish that the flow leaves tangential to the trailing edge is not necessary because at the last panel we already apply the condition that the flow is tangential. If the model is used for thick airfoil, then it is to be noted that at trailing edge, we would incorporate the flow to be tangential each of the trailing edge panels (one on the suction side and the other on pressure side). This should be modified either by removing one of these conditions and allowing the flow to be tangential to only one of the panel or by removing both of these conditions and allowing the flow to be tangential to the angular bisector of trailing edge angle. By following either of the approaches would reduce one equation from the system of equations and an additional condition that vorticity at trailing edge is zero should be incorporated.

4.2.2 Computation of loads

The system of equations formed are solved to obtain the distribution of circulation on the airfoil. The resultant aerodynamic lift can be found by using the Kutta-Joukowski theorem 3.22. The lift generated at i^{th} panel is given by

$$\Delta L_i = \rho U_\infty \Gamma_i,$$

and the pressure acting at the panel is estimated by

$$\Delta p_i = \rho U_\infty \frac{\Gamma_i}{\Delta l_i}$$

where Δl_i is the panel length. The total lift can be calculated by summing the individual lift components at each panel. An alternate approach of calculating lift is to sum up force

due to the obtained pressure distribution in the direction perpendicular to free stream. However using Kutta-Joukowski theorem is much simpler to implement. The moment acting about the leading edge due to i^{th} panel is given by multiplying the force with the corresponding moment arm length,

$$\Delta M_i = -\Delta p_i \Delta l_i x_i \cos\alpha$$

4.3 Unsteady single wake model

In this section, the unsteady single wake model used to study attached flows is presented. The unsteady Kutta condition used to determine the shed circulation is presented in section 4.3.1. Then the construction of the matrices that include the system of equations is given in section 4.3.2. the calculation of momentary pressure distribution in section 4.3.3 followed by convecting the shed wake vortex points in section 4.3.4.

In unsteady single wake model, the system of equations are solved at each time step. A similar discretization of airfoil into several straight panels, as described in section 4.2 is used. The airfoil is modeled using point vortex singularity elements placed at quarter chord point of each panel. These point vortex circulation strengths representing the airfoil form N_{pan} unknowns. The circulation shed into the wake at each time step is also modeled using point vortices and during a particular time step i, one unknown wake circulation strength Γ_{W_i} adds to the system of equations, making a total of $N_{pan} + 1$ unknowns.

4.3.1 Kutta condition

The main difference in unsteady single wake model when compared to steady model is the release of trailing edge vorticity during each time step. The strength of the vorticity released can be estimated in two ways. One of the ways that is easy to implement is to express the released vorticity in terms of vorticity developed on the airfoil. This is governed by the Kelvin's theorem as

$$\frac{\partial \Gamma}{\partial t} = 0,$$
$$\frac{\partial \Gamma_a}{\partial t} + \frac{\partial \Gamma_w}{\partial t} = 0,$$

where Γ_a is the circulation generated on the airfoil and Γ_w is circulation in the wake. Using the above equation, the circulation released from the trailing edge is given by

$$\frac{\partial \Gamma_w}{\partial t} = -\frac{\partial \Gamma_a}{\partial t} \tag{4.3}$$

While solving the first time step, there is no wake vorticity hence the above equation governs 4.3 that the circulation developed on the airfoil is released into the wake. In the consequent time steps, the effect of the shed vorticity has to be included while calculating the induced velocity at collocation points. Since, in the current time step, the strength of the wake vortices would be known in priori, the effect of these can be included in the right hand side of the system of equations. Once the circulation strength of the shed wake

vortex is known, it will remain constant in time and it would then only be convected with local flow. Applying Kelvin's theorem at any intermediate time step would then result in

$$\Gamma_a + \Gamma_{W_k} + \sum_{j=1}^{j=k-1} \Gamma_{W_j} = 0,$$

where Γ_{W_k} is the circulation shed at current time step and Γ_{W_j} are the circulations shed at the previous time steps.

The other way to estimate the vorticity released from trailing edge is to express in terms of velocities at the trailing edge which is discussed in section 3.3 given by equation 3.39. The former is used here due to its ease of implementation in the linear system of equations.

4.3.2 Formation of system of equations

The available unknowns in the unsteady single wake model are N_{pan} bound circulation strengths of point vortex singularity elements on the airfoil and one shed circulation strength at the trailing edge, a total of $N_{pan}+1$. The boundary conditions required to solve for these $N_{pan}+1$ unknown circulations are N_{pan} non penetration conditions applied at N_{pan} collocation points. Kelvin's theorem forms a additional equation governing the circulation shed during the particular time step (k) making a total of $N_{pan}+1$ equations and forming a closed set of equations to be solved. Given below is the linear system equations formed in this model and it can be clearly noticed that the only difference when compared to steady state model is the additional influence of shed wake circulation.

$$\begin{bmatrix} C_{11} & \dots & C_{1j} & \dots & C_{1N_{pan}} & D_{1W_k} \\ \vdots & \ddots & \vdots & \ddots & \vdots & \vdots \\ C_{i1} & \dots & C_{ij} & \dots & C_{iN_{pan}} & D_{iW_k} \\ \vdots & \ddots & \vdots & \ddots & \vdots & \vdots \\ C_{N_{pan}1} & \dots & C_{N_{pan}j} & \dots & C_{N_{pan}N_{pan}} & D_{N_{pan}W_k} \\ 1 & \dots & 1 & \dots & 1 & 1 \end{bmatrix} \begin{bmatrix} \Gamma_1 \\ \vdots \\ \Gamma_i \\ \vdots \\ \Gamma_{N_{pan}} \\ \Gamma_{W_k} \end{bmatrix} = \begin{bmatrix} RHS_1 + \sum_{j=1}^{j=k-1} \Gamma_{W_j} D_{1W_j} \\ \vdots \\ RHS_i + \sum_{j=1}^{j=k-1} \Gamma_{W_j} D_{iW_j} \\ \vdots \\ RHS_{N_{pan}} + \sum_{j=1}^{j=k-1} \Gamma_{W_j} D_{N_{pan}W_j} \\ -\sum_{j=1}^{j=k-1} \Gamma_{W_j} \end{bmatrix},$$

where C_{ij} are the influence terms due to the bound point vortex singularity elements as described in equation 4.1. D_{iW_k} (k-represents the current time step, $t = k\Delta t$) is defined as the influence of wake circulation shed during current (k^{th}) time step at i^{th} collocation point which can be written as

$$D_{ik} = \frac{[U_{i,W_k}, V_{i,W_k}]}{\Gamma_{W_k}} \cdot \mathbf{n} \tag{4.4}$$

4.3.3 Computation of loads

In unsteady flow, there is an additional mass of fluid which is accelerated along with the body. The fluid acceleration term is $\frac{\partial \phi}{\partial t}$ in the unsteady Bernoulli equation 3.16. The pressure difference acting on the i^{th} panel (resultant pressure considering the pressure on the upper and lower side of the panel) is given by equation 3.37 for a general vortex

distribution of $\gamma(x)$. Expressing ϕ_i in a way suitable for the current discrete vortex or lumped vortex method using equation 3.34, we get

$$\Delta p_i = \rho(V_\infty \gamma_i + \frac{\partial}{\partial t} \sum_{j=1}^{i} \Gamma_j). \tag{4.5}$$

Total lift can be found by summing the lift generated by each panel as given by equation 3.21.

$$L = \sum_{i=1}^{N_{pan}} \Delta p_i \Delta l_i \cos \alpha_i, \tag{4.6}$$

where α_i is the angle made by i^{th} panel with respect to x-axis as shown in figure 3.3.

4.3.4 Moving the wake

Before starting the calculation for next iteration, the wake vortex points should be convected according the local flow velocity experienced by the point vortex. The local flow velocity is found by summation of influence of the bound vortex elements (vortices present on the surface of the airfoil), wake vortex elements and the free stream velocity.

$$[u_{W_i}, v_{W_i}] = \sum_{j=1}^{N_{pan}} C_{ij}\Gamma_j + \sum_{k=1}^{N_{Wake-Vortices}} D_{ik}\Gamma_{W_k} + [U_\infty, V_\infty], \tag{4.7}$$

where $N_{Wake-Vortices}$ is the number of wake vortex elements present in the current time step.Once the local flow velocity at each wake vortex element is known, then they are convected using first order Euler scheme

$$\begin{aligned} x_{W_{new}} &= x_{W_{old}} + u_W * dt, \\ y_{W_{new}} &= y_{W_{old}} + v_W * dt, \end{aligned} \tag{4.8}$$

where $[u_W, v_W]$ is the matrix consisting the induced velocity components at the wake elements.

Once the wake vortices are convected, the solution is proceeded to the next iteration and is repeated till the convergence of lift coefficient whose details are given in section 5.2.

4.4 Unsteady double wake model

Double wake model is applied for the cases when flow separation is expected on the airfoil and is developed by extending the single wake model presented above. The aspects in which the double wake model differs from single wake model are discussed in this section. The main difference is the additional wake vortices released from the separation location along with trailing edge vortices. The strength of separation wake vortices are defined using the circulation equation 3.39 and the trailing edge wake is found by the application Kelvin's theorem as discussed in section 4.4.1. In the double wake model, the location of

flow separation on the surface of the airfoil is known in priori either from experiments or RANS simulations.

In unsteady double wake model, the system of equations are solved in a similar manner as in single wake model. An additional unknown circulation strength of separation wake ($\Gamma_{W_{SP}}$) is to be estimated at each time step along with trailing edge wake strength ($\Gamma_{W_{TE}}$). The unsteady kutta condition used in order to define the shed circulation strengths is discussed in section 4.4.1. The system of equations formed in this model is presented in section 4.4.2. The procedure to move the shed wake vortices is similar as in the case of single wake model and here an additional set of separation wake vortices have to be convected with the local flow.

4.4.1 Kutta condition

The amount of circulation shed in a time interval (Δt) from the separation location is given by the equation 3.39.

$$\frac{d\Gamma_{W_{SP}}}{dt} = \frac{1}{2}(V_u^2 - V_l^2),$$

where V_u is the velocity above the shear layer and V_l is below it. However this is a non linear equation and cannot be directly included into the linear system of equations. So at a particular time step, the separation wake vortex strength is defined using the information of velocity from the previous time steps potential solution. Also the lower velocity is taken to be zero. The circulation reduction factor is introduced, following the same approach of [23]. The strength of separated wake vortex is given by

$$\Delta\Gamma_{W_{SP}} = \frac{K}{2}V_u^2\Delta t. \tag{4.9}$$

The circulation reduction, K of $0.5 - 0.6$ is used. And in order to define the strength of trailing edge wake vortex, Kelvins theorem is applied

$$\frac{\partial\Gamma_a}{\partial t} + \frac{\partial\Gamma_{W_{SP}}}{\partial t} + \frac{\partial\Gamma_{W_{TE}}}{\partial t} = 0 \tag{4.10}$$

At a particular time step, the strength of separated wake is known using the information from previous time step and hence its no longer an unknown.

4.4.2 Formation of system of equations

The unknowns in the unsteady double wake model are the same as in the case of single wake model, N_{pan} bound circulation strengths and one trailing edge wake strength. The modeling of separation wake did not add a additional unknown to the system since it is a known quantity at the current time step as discusses above. The boundary conditions required to solve for these unknowns remain the same as in the case of single wake model but the application of Kelvin's theorem is modified according to equation 4.10. The

resultant system of equations are

$$\begin{bmatrix} C_{11} & \dots & C_{1j} & \dots & C_{1N_{pan}} & D_{1W_k} \\ \vdots & \ddots & \vdots & \ddots & \vdots & \vdots \\ C_{i1} & \dots & C_{ij} & \dots & C_{iN_{pan}} & D_{iW_k} \\ \vdots & \ddots & \vdots & \ddots & \vdots & \vdots \\ C_{N_{pan}1} & \dots & C_{N_{pan}j} & \dots & C_{N_{pan}N_{pan}} & D_{N_{pan}W_k} \\ 1 & \dots & 1 & \dots & 1 & 1 \end{bmatrix} \begin{bmatrix} \Gamma_1 \\ \vdots \\ \Gamma_i \\ \vdots \\ \Gamma_{N_{pan}} \\ \Gamma_{W_k} \end{bmatrix} =$$

$$\begin{bmatrix} RHS_1 + \sum_{j=1}^{j=k-1} \Gamma_{W_{TEj}} D_{1W_j} + \sum_{j=1}^{j=k} \Gamma_{W_{SPj}} E_{1W_j} \\ \vdots \\ RHS_i + \sum_{j=1}^{j=k-1} \Gamma_{W_{TEj}} D_{iW_j} + \sum_{j=1}^{j=k} \Gamma_{W_{SPj}} E_{iW_j} \\ \vdots \\ RHS_{N_{pan}} + \sum_{j=1}^{j=k-1} \Gamma_{W_{TEj}} D_{N_{pan}W_j} + + \sum_{j=1}^{j=k} \Gamma_{W_{SPj}} E_{N_{pan}W_j} \\ - \sum_{j=1}^{j=k-1} \Gamma_{W_{TEj}} - \sum_{j=1}^{j=k} \Gamma_{W_{SPj}} \end{bmatrix},$$

where E_{ij} are the influence terms of separated wake elements similar to D_{ij} as defined earlier. Here notice the summation over trailing edge influence terms in the matrix on the right hand side is only till $k-1$, because the strength of trailing edge vortex released during the current time step is an unknown.

4.4.3 Computation of loads

The pressure distribution in the region of attached flow is calculated using equation 3.17. There is head jump Δh across the separated shear layer, as discussed in section 3.2.2, which is to be considered when calculating the pressure in the separated region using equation 3.20, where Δh given by equation 3.41 is approximated as

$$\Delta h = \frac{\partial \Delta \Gamma_{W_{SP}}}{\partial t} + \frac{\partial \Delta \phi_{SP}}{\partial t}, \tag{4.11}$$

where $\Delta \phi_{SP}$ is change in potential across the separated shear layer.

4.4.4 Moving the wake

The wake vortex points are convected in the same way as in the case of single wake analysis presented in section 4.3.4. But the only difference is in this case there is additional wake shed from the separation location whose influence is to be considered while estimating the induced velocity.

Once the local flow velocity at each wake vortex element is known, then they are convected using first order Euler scheme

$$\begin{aligned} x_{W_{SP_{new}}} &= x_{W_{SP_{old}}} + u_{W_{SP}} * dt, \\ y_{W_{SP_{new}}} &= y_{W_{SP_{old}}} + v_{W_{SP}} * dt, \\ x_{W_{TE_{new}}} &= x_{W_{TE_{old}}} + u_{W_{TE}} * dt, \\ y_{W_{TE_{new}}} &= y_{W_{TE_{old}}} + v_{W_{TE}} * dt, \end{aligned}$$

where $[u_{W_{SP}}, v_{W_{SP}}]$ is the matrix consisting the induced velocity components at the separation wake elements and similarly $[u_{W_{TE}}, v_{W_{TE}}]$ is velocity matrix of the trailing edge wake.

Once the wake vortices are convected, the solution is proceeded to the next iteration.

Chapter 5

Numerical results and discussion

5.1 Validation of Steady State Model (SSM)

In this section the steady state model developed using point vortex singularity elements is validated using flat plate and cambered plate whose steady state analytical results are available in [23].

5.1.1 Flat plate analysis

A flat plate geometry, shown in figure 4.1 is used for the purpose of validation since the analytical results are readily available for the comparison. In this section a flat plate is considered at a fixed angle of attack and the convergence of the obtained results is discussed. Then the aerodynamic coefficients are compared with the analytical results and the convergence of the model with respect to panel density is discussed.

For the analysis performed in this section, the free stream velocity used is unity in the direction of x-axis and the flat plate is rotated according to the angle of attack described in the particular case.

Fixed angle of attack

The flat plate is discretized into straight panels and several cases are studied with increasing number of panels in order understand the convergence of circulation distribution and resultant pressure distribution. The pressure on the flat plate is calculated using Kutta-Joukowski theorem as discussed in section 3.2.3. The flat plate is fixed at 5° angle of attack and convergence study has been carried.

The circulation distribution obtained at 5° for various number of panels from 40 to 500 is shown in figure 5.1. It can be noticed that circulation curve doesn't seem to be converging because with the increase in number of panels, the number of point vortex singularity

elements increase and in order to create the same amount of total circulation ($\sum_{i=1}^{i=N_{pan}} \Gamma_i$), the distribution of circulation changes according to the number of panels. This is verified from the calculation of total circulation (in other terms, the amount of lift generated($\propto \sum_{i=1}^{i=N_{pan}} \Gamma_i$)) which remains same for all the cases. Also this is evident from figure 5.1 that circulation at a given chord location decreases with increasing number of panels, curve obtained for 40 panels lies above the curve with 80 panels and so on. Hence circulation distribution is not considered in order to comment on number of panels required for accuracy of the solution. It can be noticed that the circulation goes to zero at the trailing

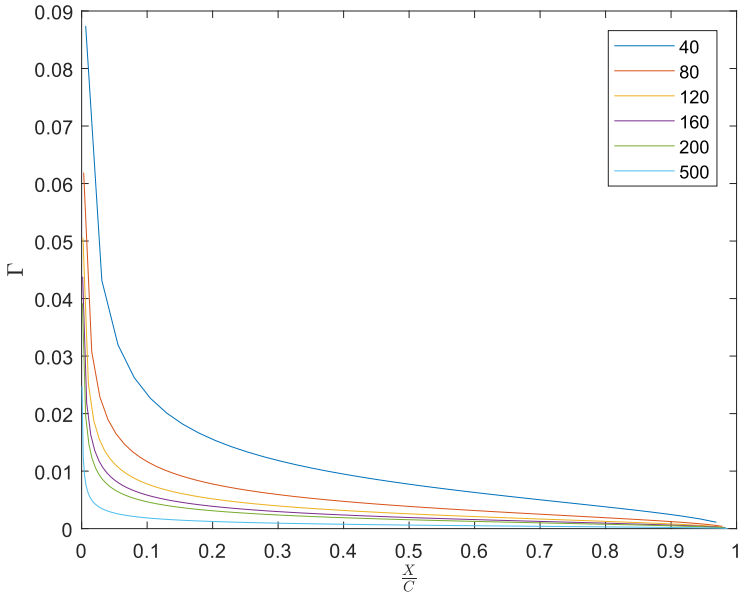

Figure 5.1: Circulation distribution on a flat plate at 5° angle of attack for various cases with increasing number of panels.

edge of the flat plate. This is a result of the Kutta condition that flow has to be tangential to the trailing edge which is not specifically applied but it is a result of no penetration condition at the trailing edge panel in this model. Also applying the definition of shed circulation 3.39, it can be derived that velocity above and below the trailing edge plate are equal and no circulation is shed and the solution is a steady state solution.

The pressure coefficient distribution obtained at the same angle of attack for similar cases of increasing number of panels is given in figure 5.2. From pressure coefficient distribution plot 5.2, it can be noticed that for all the curves fall close to each other except at the leading edge. This is clearly shown in figure 5.3. From the analytical solution of flat plate pressure distribution [23], we know that solution becomes singular and the model is not accurate. In the remainder of the chord length, the pressure distribution is accurately predicted by the model, even with 40 panels, apart from leading edge region. But with 40 panels, C_P curve is not smooth to a greater extent near the leading edge and is way off from the curve obtained for 500 panels. In order to conclude on the number of panels required for accurate prediction, considering the C_P distribution plots 5.2, 5.3, it is decided to choose 120 panels, since the C_P curve obtained for 120 panels is smoother than the cases with of 40 and 80 panels.

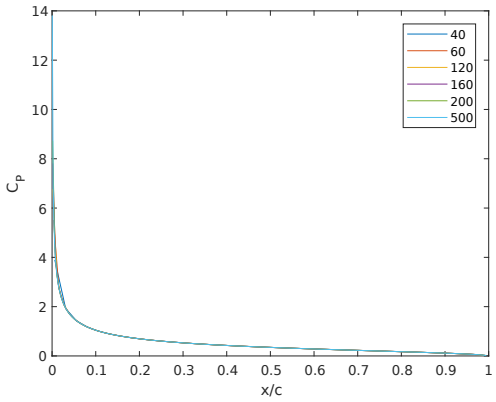

Figure 5.2: Coefficient of pressure distribution on flat plate at 5° angle of attack for various cases with increasing number of panels

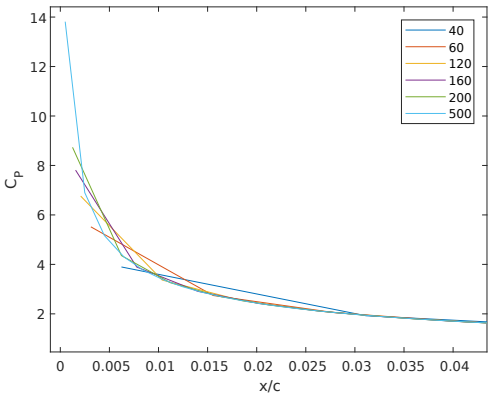

Figure 5.3: Zoom in at the pressure distribution near leading edge.

Lift and moment polars comparison with analytical results

The flat plate is discretized in 120 straight panels and lift and moment coefficients are obtained for a range of angle of attacks $0° < \alpha < 10°$. But even for very small number of panels such as 2, it is observed to arriving at the same value to lift coefficient as with 120 panels. Hence depending on the interest of user, number of panels can be chosen to be higher to arrive at accurate pressure distribution. The coefficient of lift obtained from SSM is compared to the analytical solution in figure 5.4. The lift and moment coefficients of flat plate are analytically given by [23]

$$C_L = 2\pi\alpha,$$
$$C_{M_0} = -\frac{\pi}{2}\alpha.$$

The lift polar predicted by SSM falls on the top of the polar obtained from analytical solution. In the above mentioned analytical solutions of lift and moment coefficients, the angle of attack is assumed to small $\alpha << 1$ and $\sin\alpha$ is approximated to α. If such approximated expression is used, as the angle of attack increases, this approximation starts to deviate more and results in a marginal deviation at high angle of attacks. Here the polars obtained from SSM are compared to exact analytical solutions and such a deviation is not observed.

The coefficient of moment about the leading edge of flat plate obtained from SSM is compared with the analytical solution, as shown in figure 5.5. Even with very less number of panels (≈ 5), we arrive at same lift and moment polars. So it can be concluded that if the interest of the user is in the pressure distribution, ≈ 120 panels should be used to arrive at accurate pressure distribution except at the leading edge. And if lift and moment coefficients are of interest then less number of panels (in the case of flat plate even with one panel accuracy) would suffice.

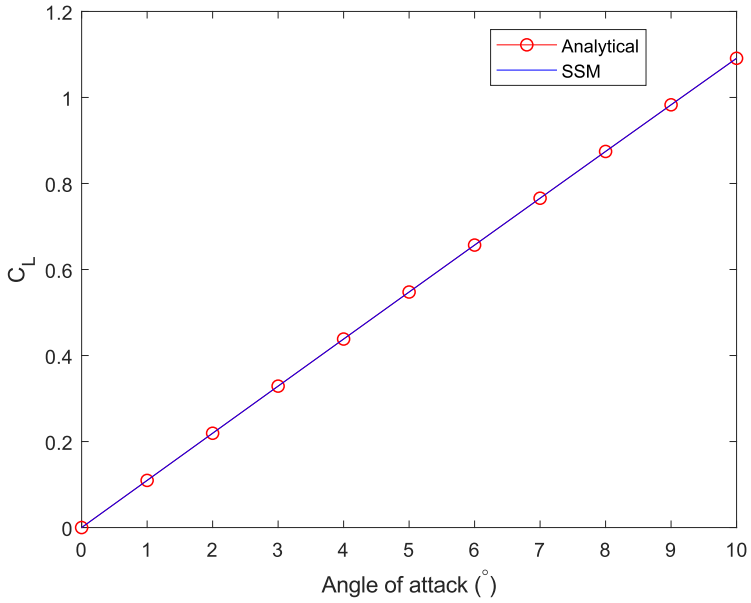

Figure 5.4: Lift coefficient (C_L) of the flat plate for range of angle of attacks $0° \leq \alpha \leq 10°$.

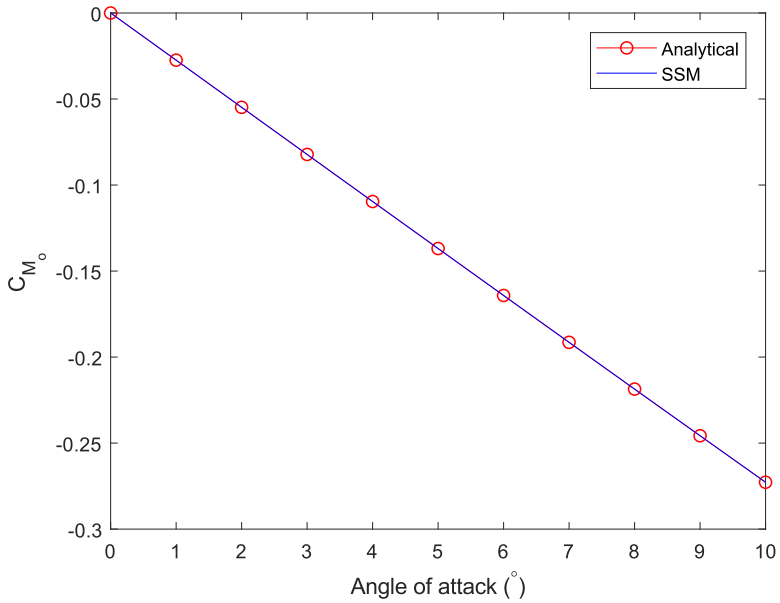

Figure 5.5: Moment coefficient (C_{M_0}) about the leading edge of the flat plate for range of angle of attacks $0° \leq \alpha \leq 10°$.

5.1.2 Cambered plate analysis

The cambered plate used for the following analysis is parabolic arc airfoil as shown in figure 5.6, whose camber line equation is given by

$$\eta(x) = 4\epsilon\frac{x}{c}[1 - \frac{x}{c}]$$

The analytical pressure distribution for this type of cambered plate assuming small values of ϵ is given by

$$C_p = 4\sqrt{\frac{c-x}{x}}\alpha + 32\frac{\epsilon}{c}\sqrt{\frac{x}{c}(1-\frac{x}{c})}$$

and the corresponding aerodynamic coefficients are given by

$$C_l = 2\pi(\alpha + 2\frac{\epsilon}{c}),$$
$$C_{M_0} = -\frac{\pi}{2}(\alpha + 4\frac{\epsilon}{c})$$

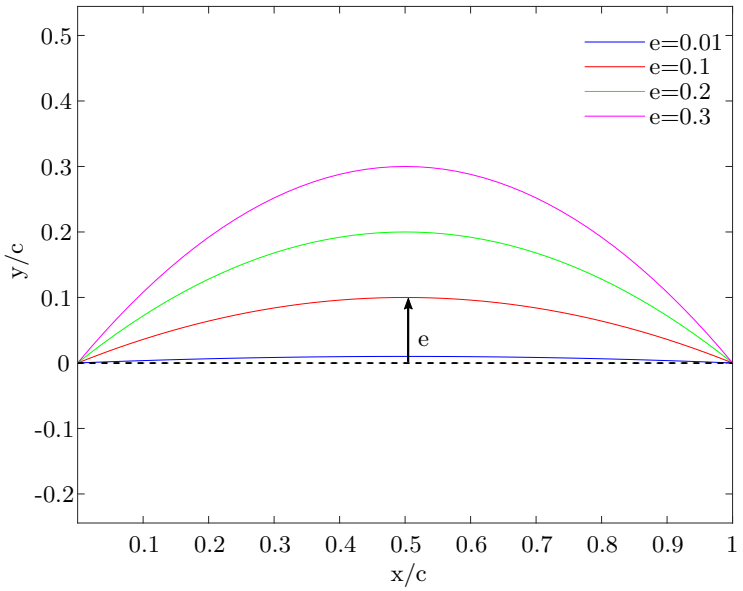

Figure 5.6: Cambered plate

Fixed angle of attack

A similar analysis, as conducted on flat plate, on various cambered airfoil profiles with increasing camber (e) at a fixed angle of attack of 0° resulted in a pressure distribution given in figure 5.7. It can be noticed that the analytical solution gives good approximation only for small camber ($e \leq 0.1$). With increase in camber, the analytical solution deviates more. This is because the analytical solution is derived assuming small disturbance approximations and is ideal to use only for low cambered airfoils.

Lift and moment polars comparison with analytical results

The lift and moment polars obtained from the analysis conducted for a range of angle of attacks ($0° \leq \alpha \leq 10°$) for cambered airfoils of increasing camber are compared to

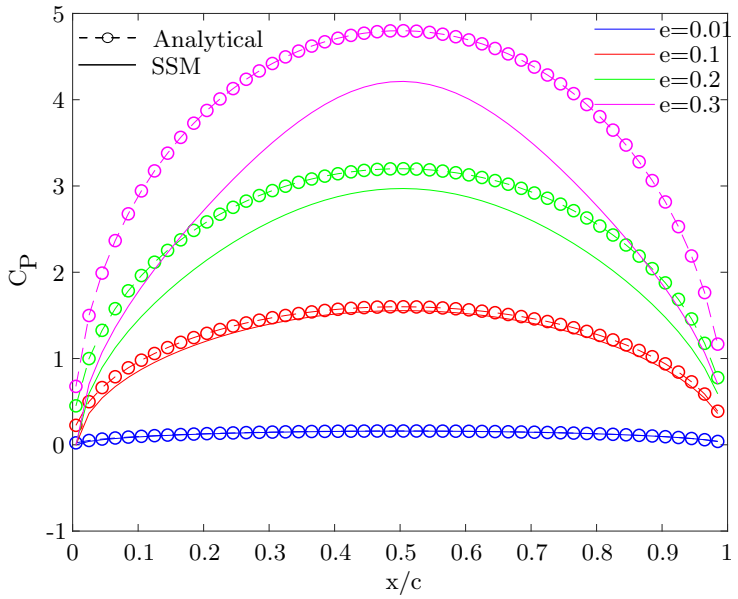

Figure 5.7: Pressure distribution

analytical solution. Figure 5.8 is the comparison of lift polars obtained from SSM to analytical solution. It can be seen that with increase in camber, the analytical solution over predicts the lift. Considering the applicability of analytical solution, as explained, the lift polar falls close to SSM solution for low cambered plate. It can be observed that with the increase in camber, the lift generated by the plate increases as expected and the slope of the polar remains the same. Similarly from figure 5.9, it can be noticed that for low cambered airfoils, the moment polar obtained from analytical solution is close to the results from SSM and deviates with increase in camber.

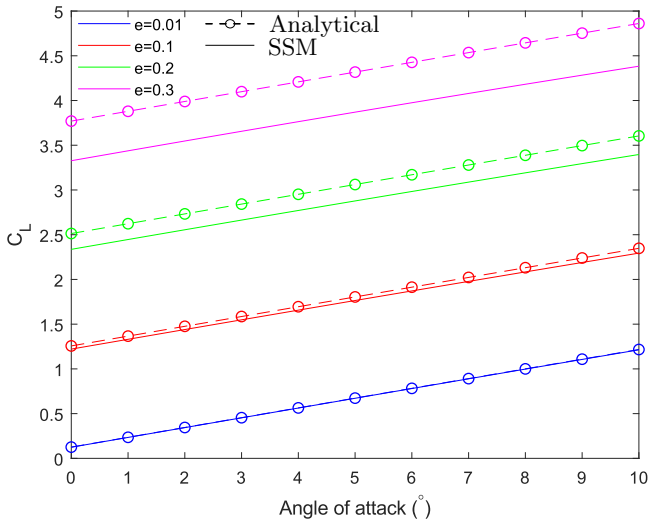

Figure 5.8: Lift coefficient (C_{M_0}) of various cambered plates for range of angle of attacks $0° \leq \alpha \leq 10°$.

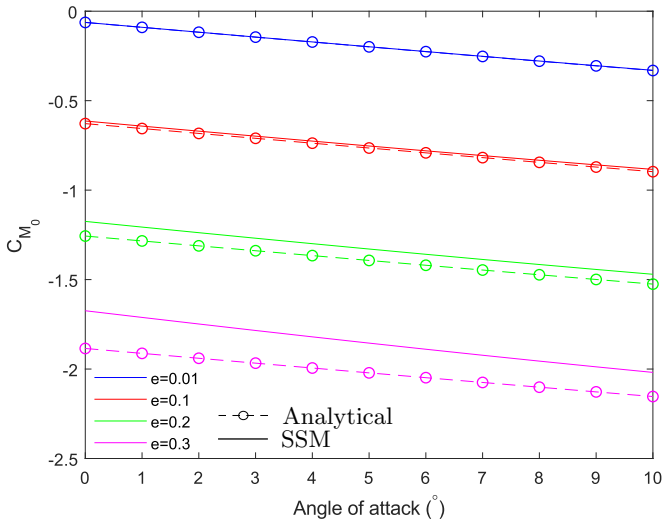

Figure 5.9: Moment coefficient (C_{M_0}) about leading edge of various cambered plates for range of angle of attacks $0° \leq \alpha \leq 10°$.

5.2 Validation of unsteady single wake model (USWM)

5.2.1 Flat plate analysis

In this section, the USWM developed is tested using the case of impulsively started flat plate. The analysis at fixed angle of attack is presented in this section and lift generated as a function of time is validated with Wagner function 3.38. For the part of analysis during which pressure distribution is not considered, less number of panels such as 10 panels is used so that computational time would be less. And for the analysis that considers pressure distribution, flat plate is discretized into 120 panels.

At a fixed angle of attack of 5°, the flat plate is impulsively started from rest. The reduced time step $\frac{\Delta t U_\infty}{c} = 0.05$ is employed for this analysis.

The lift generated by impulsively started plate has two components, one is due to the circulation developed on the airfoil and other due to the fluid acceleration term as discussed in section 3.2.6. The ratio of lift generated by impulsively started plate to the steady state lift is plotted along with the Wagner function in figure 5.10. It can be noticed that at time t=0+, high amount to lift is generated. This is due to the fluid acceleration term which is high because of the impulsive starting behavior. The acceleration at the very instinct of the start is high and it is observed that as the reduced time step is decreased, the peak in the lift generated becomes even higher. The circulation on the airfoil is also plotted in the same figure 5.10. At time t=0, there is no circulation on the flat plate because it is still in rest and as time progresses, the circulation increases but is very less than steady state value. This implies that the lift generated in this transient stage is mostly due to fluid acceleration. As a result the lift drops immediately after this impulsive starting behavior. This is due to the influence of starting wake vortex on the flat plate, shown

in figure 5.11. As this starting vortex convects away, its influence on the airfoil reduces. After a certain time, the increase in the circulation becomes slow and is asymptotic to the value of steady state circulation. The growth of circulation to the exact steady state value extends to infinity, when the influence of starting vortex becomes negligible. The

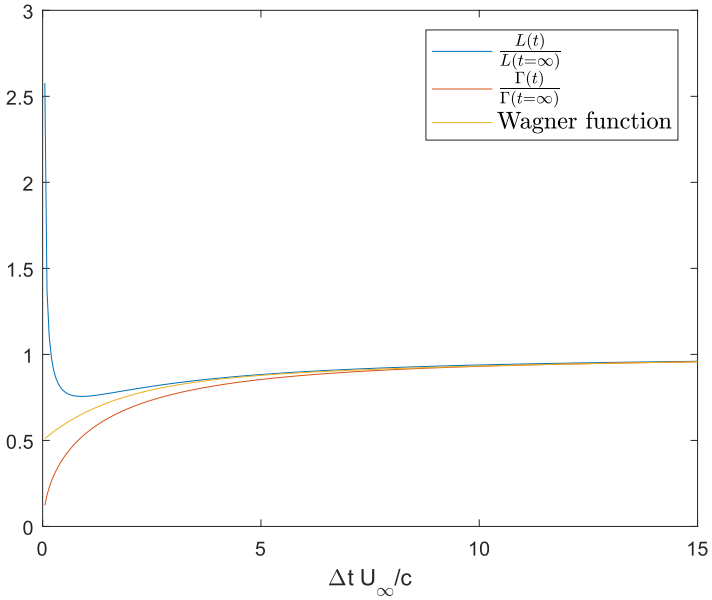

Figure 5.10: Ratio of lift generated with the corresponding steady state lift for a impulsively started flat plate at 5° angle of attack validated with the Wagner function. Ratio of circulation with respect to steady state value is also plotted. Reduced time step $\frac{\Delta t U_\infty}{c} = 0.05$ is used for this analysis.

lift produced also becomes asymptotic to the steady state value and its transient growth extends to infinity. It can also be concluded that at this transient growth stage, estimation of lift with out including the fluid acceleration term, i.e. considering only the circulation (using Kutta-Joukowski theorem), results in accurate estimation. The ratio of circulation shed to steady state circulation on the airfoil with time is shown in figure 5.11. It can be clearly seen that the amount of circulation shed reduces as time progresses and it has maximum effect only during the initial phase and becomes insignificant at later times. The circulation shed from the flat plate have negative (counterclockwise) values, hence the wake is rolled up as shown in figure 5.12. For the purpose obtaining acceptable solution a criteria with respect to the difference of unsteady solution of lift coefficient with steady state value is chosen. A study in order to note the time taken to reach certain level of percentage difference is performed. In this study the reduced time step is fixed to 0.1s. The figure 5.13 shows the time taken to reach particular level of tolerance. It can be noticed that time taken at lower tolerance levels is higher, i.e. time taken to reach 5% difference from 10% is less when compared to reach 1% from 5%. Hence a compromise has to be made with respect to computational time and accuracy because time taken increases drastically if very high accuracy is needed. At this stage, it is decided that if the difference is less than 2%, then solution is considered to be steady state. In order to estimate the pressure distribution on the flat plate and compare to the steady state

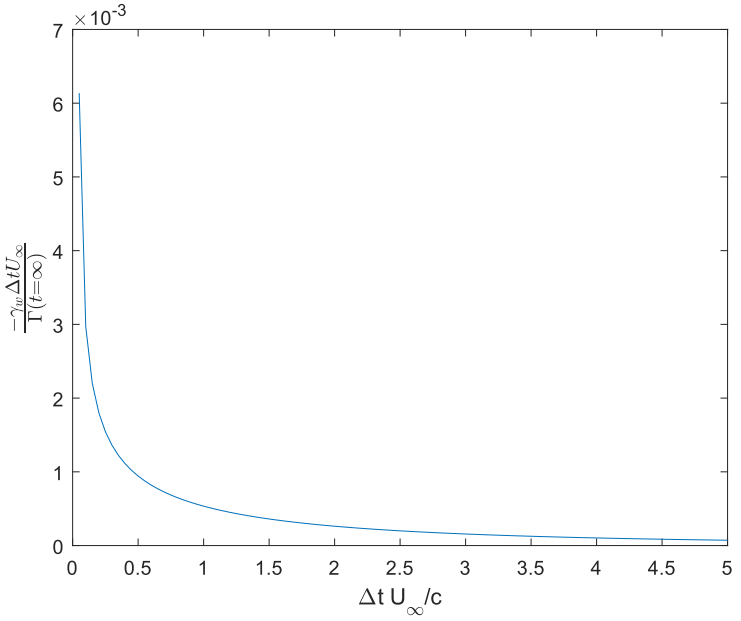

Figure 5.11: Ratio of wake circulation strength to steady state airfoil circulation for impulsively started flat plate at $5°$ angle of attack at reduced time step $\frac{\Delta t U_\infty}{c} = 0.05$

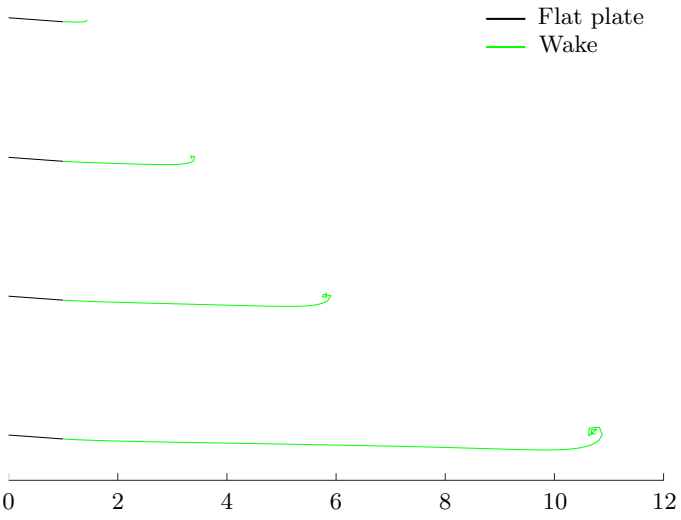

Figure 5.12: Wake formed by impulsively started flat plate at $5°$ angle of attack at reduced time step $\frac{\Delta t U_\infty}{c} = 0.05$ and after time = 10s

distribution, it is discretized into 120 panels. The obtained pressure coefficient distribution after it reaches steady state (after time = 20s) is plotted along with the distribution obtained from steady state in figure 5.14. Both the curves fall close to each other and the curve from USWM falls lower to the curve due to SSM as expected, due to starting

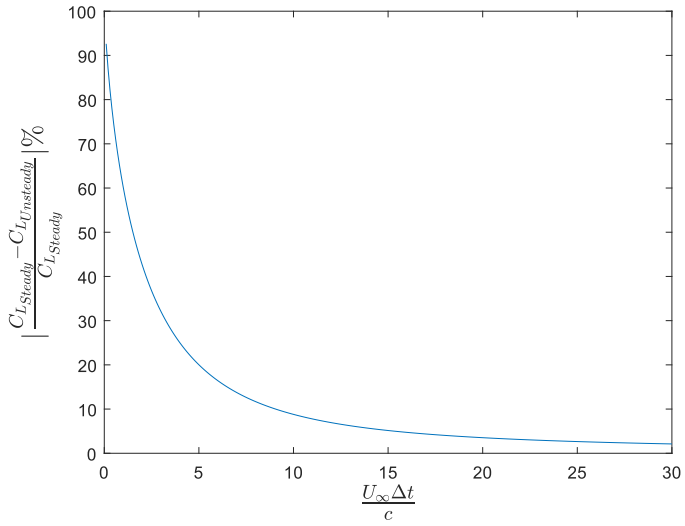

Figure 5.13: Percentage difference between C_L obtained from SSM and USWM with respect to time. The reduced time step is 0.05s.

vortex influence as discussed above. The difference between the curves reduces as time progresses and a decision has to be made in order to have a acceptable accuracy in the solution.

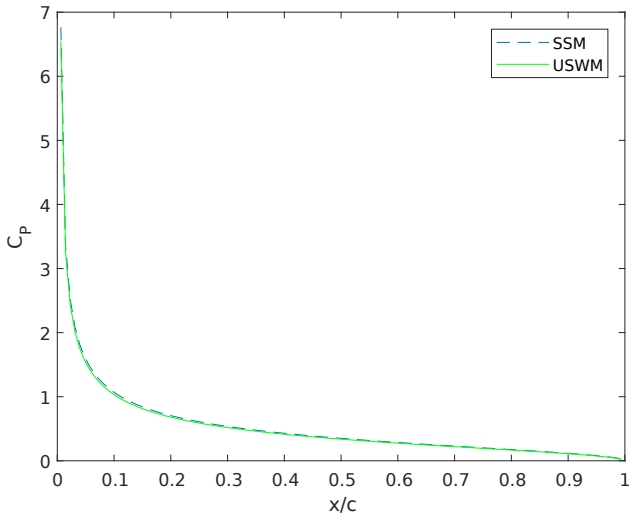

Figure 5.14: Coefficient of pressure distribution obtained from steady state model (SSM) and unsteady single wake model (USWM) after 20 seconds

5.2.2 Cambered plate analysis

For this analysis, cambered plate with $e = 0.1$ is considered at an angle of attack of 5°. A reduced time step of 0.1 is chosen the analysis. The coefficient of lift obtained from

the steady state model for the same is 1.7523. Figure 5.15 shows the convergence of lift coefficient with time. It can be noticed that the percentage difference between steady and unsteady C_L reduces to a accuracy of 2% after 25s from figure 5.16. The wake shed

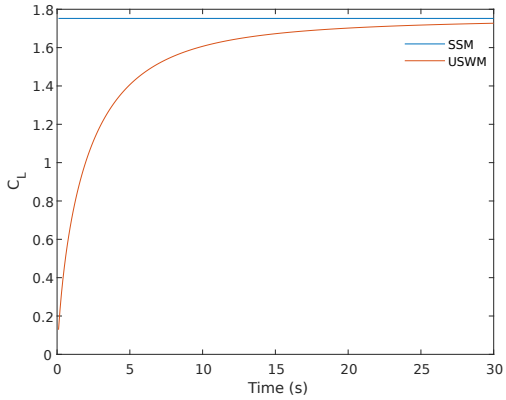

Figure 5.15: Coefficient of lift of cambered plate at 5° angle of attack converging towards the steady state solution.

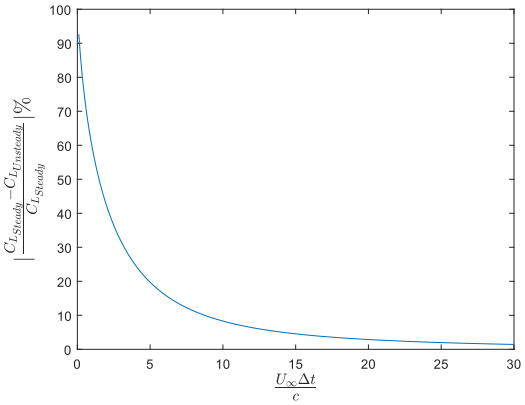

Figure 5.16: Percentage difference between C_L obtained from SSM and USWM with respect to time.

behind the cambered in this configuration is shown in figure 5.17. It can be seen that the starting vortex is convected away, and as its influence on the plate reduces and flow reaches steady state when this influence reduces to zero which theoretically happens when starting vortex is convected far away.

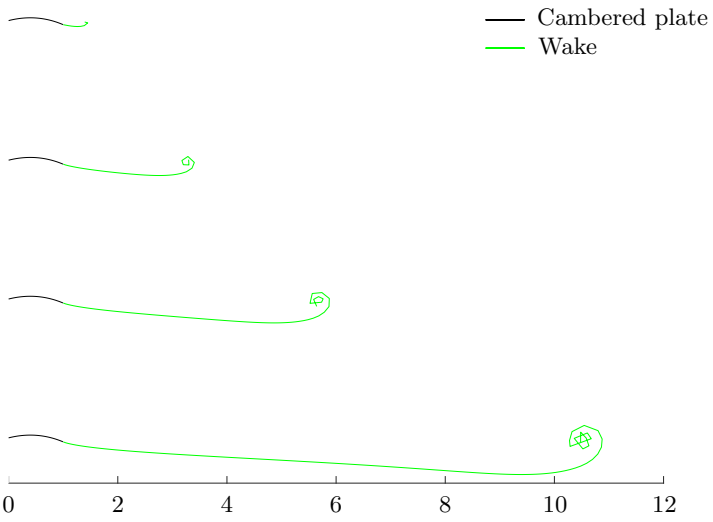

Figure 5.17: Wake formed by impulsively started cambered plate at 5° angle of attack at reduced time step $\frac{\Delta t U_\infty}{c} = 0.1$ and after time = 10s.

5.3 Modeling challenges in unsteady double wake model

The double wake model developed in this study is used to validate the case of leading edge flow separation that occurs at high angle of attack on a flat plate since this case is readily available for comparison from [22]. The main difficulty faced during the implementation of double wake model is defining the location of separation wake vortex and its strength.

The location of the separation wake vortex is unknown in the current iteration. A guess of the location has to be made and it should not be close bound vortex at the leading. The location of the separation vortex is taken at a distance from the leading edge of flat plate in the direction of free stream as shown in figure 5.18. If the location is close to

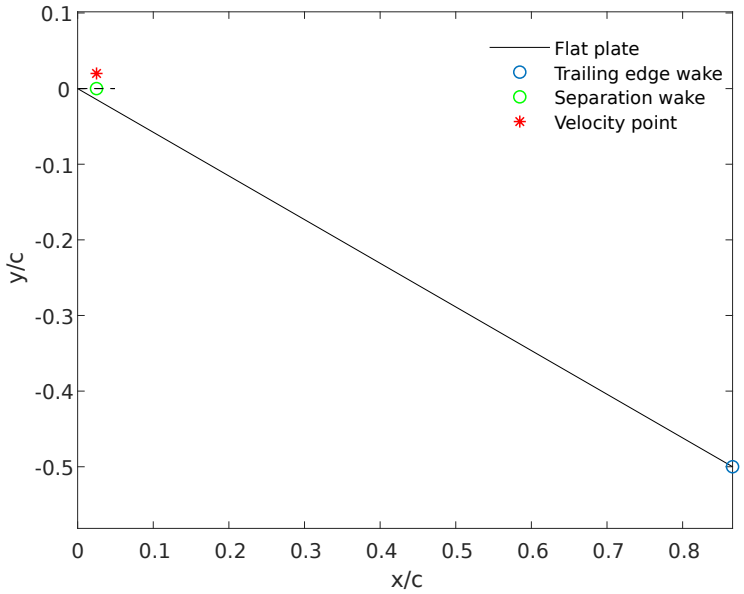

Figure 5.18: Location of the separation wake and the velocity point to estimate the strength defined at the leading edge of the flat plate.

the bound vortex point, the separation vortex experiences a high velocity because the strength of the bound vortex at the leading edge is relatively high as is estimated for flat plate at 5° in figure 5.1. The strength of the separation wake vortex is given by equation 4.9 in terms of velocity above the shear layer. This is non linear equation which cannot be included in the linear system of equations and hence solving for the separated wake vortex strength is not possible. The strength of latest separated vortex is therefore determined from the information of velocity from the previous iteration. The location of this velocity point, as shown in figure 5.18 at which the information of flow velocity is used to estimate the strength of the separated wake element is not exactly known either. Theoretically, in order to define the strength, the velocity just above the shear layer has to be considered. But velocity at a point extremely close to the separated vortex would result in a very high magnitude due to the singular nature of the vortex element. This problem can be rectified by choosing a core radius for the wake vortices. However the magnitude of velocity changes with distance from the shear layer. As a result, the strength of the wake vortex changes depending on the location of point to measure the velocity.

Several attempts have been made by changing the location of separation point and at

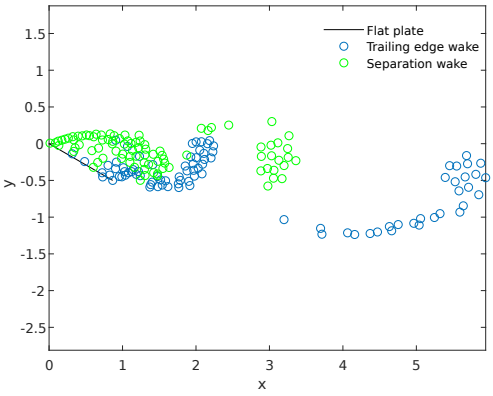

Figure 5.19: Double wake simulation for a reduced time step of 0.05s. The formation of periodic wake shedding can be observed.

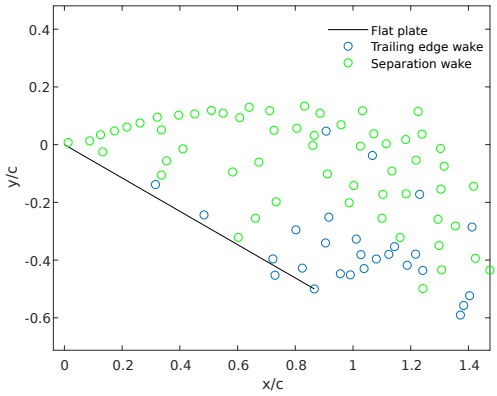

Figure 5.20: Wake elements close to and crossing the flat plate.

each attempt the location of velocity point to define the strength is also varied. These attempts didn't result in successful double wake model. It is also noticed that during certain time, the wake vortices come close and cross the flat plate as shown in figure 5.20 which is unphysical. When the wake vortices come close to the bound vortex, it experiences high velocity due to the singular nature of the vortex element. So the wake vortex is convected to far away when moved for the next time step. Also it is observed that when the wake elements reach close to each other, they are subject to high velocities and are moved far.

5.3.1 Restriction on time step

In order to understand the effect of separation wake elements on the pressure distribution of the airfoil, flow separation on a cambered plate of e=0.2 at 15° angle of attack is simulated using double wake model. The pressure distribution is obtained after post processing including the head jump at the separation location, as discussed in section 3.3. The cambered plate is discretized into 50 panels and time step is varied from 0.01s to 0.1s and the changes in pressure distribution is studied. It is noticed that near the separation location the shed wake elements move close to the plate as shown in figure 5.23. When a time step of $\Delta t \geq 0.02$ is used, jumps in the pressure distribution are observed as given in figure 5.21. But when a time step of $\Delta t = 0.01$ is used, smooth pressure distribution is observed as given in 5.22. The appropriate time step to choose is a function of the discretized panel length ($\frac{1}{N_{pan}}$). Then shed wake elements near the separation location should not move more than the one panel length. If it moves more than length of a panel and still stays close to the airfoil, then there would be few panels which experience less influence of wake elements. In the above mentioned analysis, there are 50 panels i.e the length of each panel is $\approx \frac{1}{50} = 0.02$. The distance traveled by wake element in a time

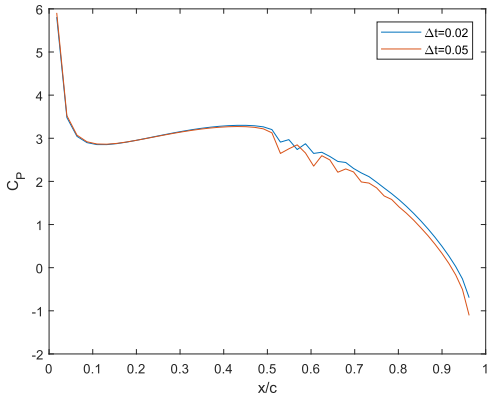

Figure 5.21: Double wake simulation for a reduced time step $\Delta t > 0.01s$.

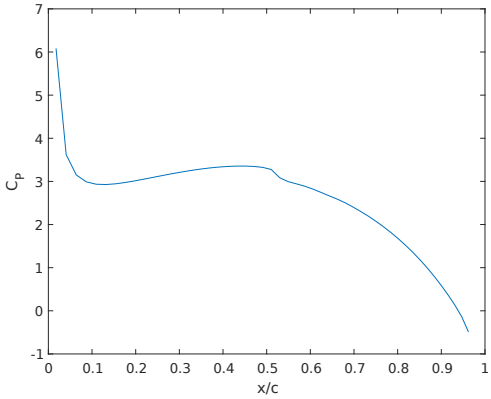

Figure 5.22: Pressure distribution obtained for $\Delta t = 0.01s$.

interval can be approximated as $V_\infty.\Delta t$ should be less than one panel length, which gives

$$\Delta t < 0.02s.$$

If the panel density increases then the appropriate time step reduces and results in higher computational time. Hence for double wake model, higher panel density is not appropriate and lowering panel density assists the analysis with relatively large time step as explained.

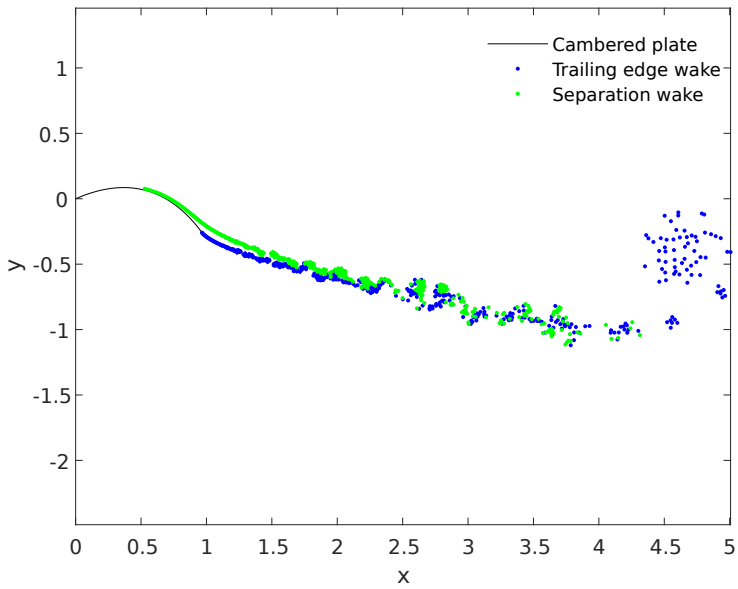

Figure 5.23: Separation wake elements close the cambered plate.

5.3.2 Linear distribution of vorticity panel method

The non linear equation of shed circulation 3.39 can be linearized if a continuous distribution of vorticity is used to model the wake instead of discrete vortex. Applying the definition of circulation 3.8 to a constant distribution of line vortex γ of length dl as shown in figure 3.4, we get

$$\Gamma = \int_S \zeta \cdot \mathbf{ds} = \gamma dl. \tag{5.1}$$

Here the idea is to model shed wake using constant strength vortex panel of strength γ. We know that the circulation emanating from the separation location is given by equation 3.39, which can be written as

$$\begin{aligned} \Delta\Gamma_{SP} &= \frac{1}{2}(V_u^2 - V_l^2)\Delta t, \\ &= (V_u - V_l)\frac{(V_u + V_l)}{2}\Delta t \end{aligned}$$

Using the equations that relate vorticity distribution to the velocity around the distribution mentioned in section 3.2.6, we can write

$$\begin{aligned} \gamma_{SP} &= V_u - V_l, \\ dl &= \frac{(V_u + V_l)}{2}\Delta t \end{aligned} \tag{5.2}$$

Using these set of equations, the shed vorticity at the separation location can be solved for by including in the linear system of equations in the current time step unlike the previous approach with the discrete vortex model. The same approach can be applied for the trailing edge shed vorticity. This type of formulation is commonly used in unsteady panel methods [1],[35]. This is also referred as unsteady kutta condition. However implementing the condition for shed vorticity in terms of velocities is straight forward approach. We can express the velocities above and below the shear layer as a function of local vorticity strengths on the airfoil and one can arrive at the simplified kutta condition which is easy to implement, as used in various unsteady panel methods that model flow separation [30], [32].

For the purpose of implementing such a model, a steady state and unsteady single wake models for airfoil with linear distribution vortex panel method are developed and validated whose results are presented in appendix A. The main difference noticed between the discrete vortex model and distribution of vorticity models is the implementation of Kutta condition.

In the steady state discrete vortex model there is no additional Kutta condition implemented since the condition is inherently applied at the trailing edge panel that the flow has to be tangential and the vorticity at the trailing edge becomes zero as shown in figure 5.1. However for the later model, there are $N + 1$ unknown vortex strengths at $N + 1$ nodes on airfoil. The additional condition of

$$\gamma_1 + \gamma_{N+1} = 0,$$

vorticity at the trailing edge should be zero is implemented.

In the single wake discrete vortex model, the shed circulation at th trailing edge is determined by the application of Kelvin's theorem. In linear distribution vortex panel method, there are $N+2$ unknown vortex strengths including the shed vorticity at trailing edge. The Kutta condition at trailing edge changes to

$$\gamma_1 + \gamma_{N+1} = \gamma_{TE},$$

where γ_{TE} is the shed vorticity at trailing edge. Kelvin's theorem closes the system of equations with $N+2$ equations and $N+2$ unknowns.

Double wake model using distribution of vorticity is developed from the validated single wake model. Now the location of separation point is considered to be known and wake is shed. In this model, the separation wake is modeled using constant strength vortex element and is convected in the form of discrete element in the next time iterations. The strength of separation wake vorticity is a new unknown which adds to a total of $N+3$ unknowns. At both separation locations, the condition of releasing the available vorticity into the flow is implemented. The vorticity at the location next to separation location is hence made zero. Alternatively if the strength of wake vortices are defined using velocity approach similar to [1], the boundary condition at separation changes. In the later case, zero velocity on the airfoil panel next to separation location should be implemented. The boundary conditions in both of these approaches are summarized in the table 5.1 below. However implementation of strength of wake vortices in terms of velocities requires

Approach 1	Approach 2
N-non penetration conditions	N-non penetration conditions
$\gamma_{W_{SP}} = \gamma_{SP}, \gamma_1 + \gamma_{N+1} = \gamma_{TE}$	$\gamma_{W_{SP}} = u_{SP-}, \gamma_{TE} = u_1 - u_{N+1}$, where u_{SP-} is the velocity on the airfoil panel just ahead of separation location, u_1, u_{N+1} are the velocities at trailing edge panels, [1]
$\gamma_{N+1} = 0$	$u_{SP+} = 0$, where u_{SP+} is the velocity on the airfoil panel lying after the separation location, [1]
Kelvin's theorem implementation	Kelvin's theorem implementation

Table 5.1: Boundary conditions identified for double wake model

additional computation of velocities and relatively not straight forward. The schematic representation of the model developed following approach 1 is given in figure 5.24. Using this approach the length and orientation of wake panels are given by

$$l_{SP} = \frac{|\gamma_{SP}|}{2},$$
$$l_{TE} = \frac{|\gamma_{TE}|}{2},$$
$$\theta_{SP} = \tan^{-1}\left(\frac{v_{W_{SP}}}{u_{W_{SP}}}\right),$$
$$\theta_{TE} = \alpha_1,$$

where $v_{W_{SP}}, u_{W_{SP}}$ are the velocity components evaluated at midpoint of separation wake panel and α_1 is angle of the trailing edge panel on pressure side. There are only $N+3$

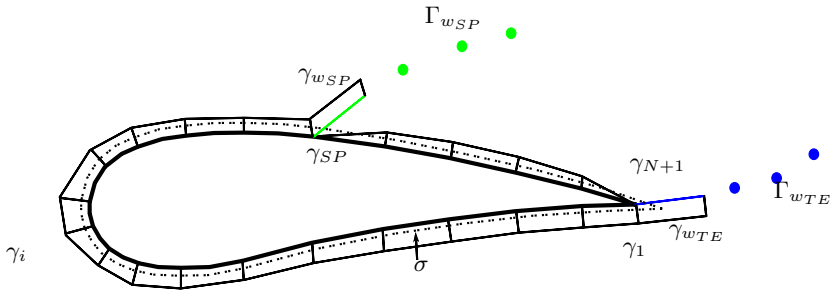

Figure 5.24: Schematic representation of double wake model developed using linear distribution of vorticity.

unknowns, $N+1$ vortex strengths on the airfoil and 2 shed wake vortex strengths. Hence a additional unknown of constant strength source is used all along the length of the airfoil, as shown in figure 5.24. A initial guess of the length of wake elements has to be made and each time step consists of sub iterations for the convergence of length and strength of the wake vortex to a convergence limit. In this case the convergence limit is chosen to be 10^{-4}.

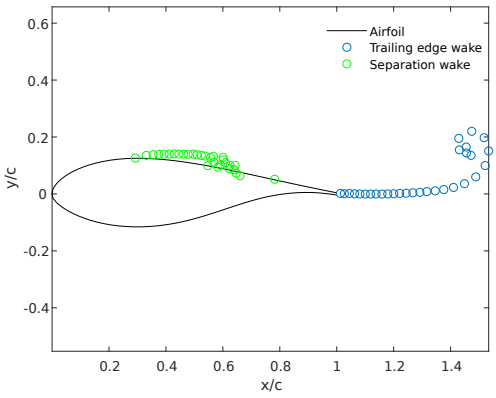

Figure 5.25: Double wake simulation for a reduced time step of 0.02s.

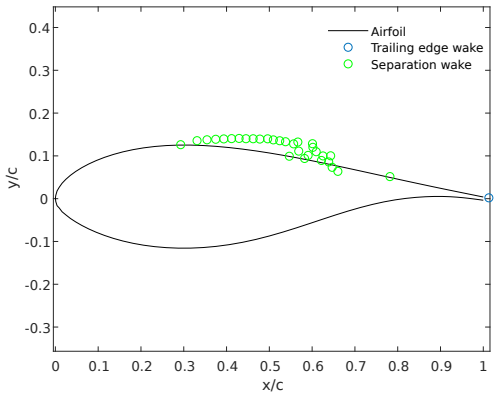

Figure 5.26: Wake elements close to and crossing the airfoil.

The simulation for the airfoil FFA_W3_241 at 17° angle of attack for time step of 0.02s, the wake vortices move close and enter the airfoil surface. Such a double wake simulation has similar issues as the discrete vortex model. The wake elements come close to the bound vortex distributions and cross the solid boundary on the airfoil, as shown in figure 5.26 which is unphysical. So we can expect, the solver when used to simulate flow reattachment results in the penetration of wake vortices into the airfoil surface. The pressure distribution obtained in such an unphysical scenario is given in figure 5.27 which shows the influence of vortices that penetrate. In an attempt to convect the wake vortices quickly downstream, the time step is increased to 0.1s. The double wake model is used to analyze separated flow over a thick airfoil FFA_W3_241 at 21° angle attack where separated flow is expected. The separation location is taken from [26] and pressure distribution obtained from such a simulation is given in figure 5.30. The lift coefficient

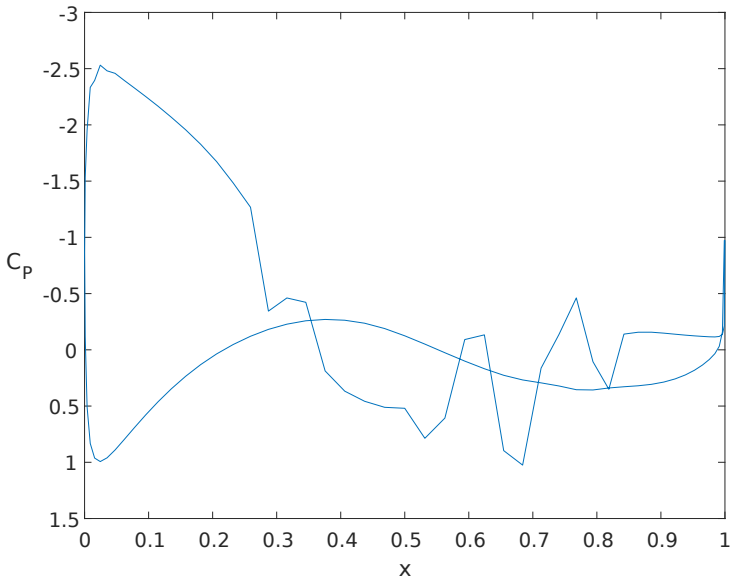

Figure 5.27: C_p distribution for the airfoil FFA_W3_241 at 17° angle of attack for time step of 0.02s.

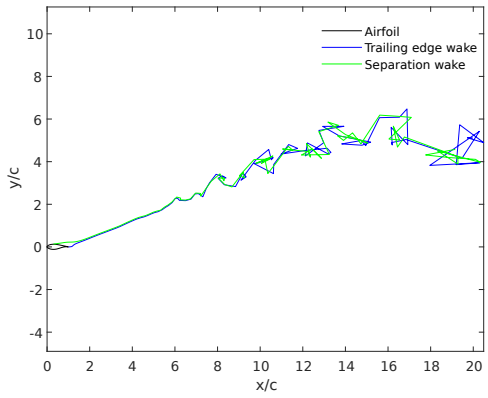

Figure 5.28: Wake formed from the double wake simulation for airfoil FFA_W3_241 at 21° angle of attack for time step of 0.1s.

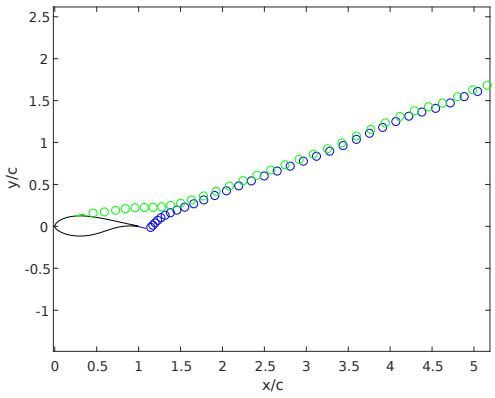

Figure 5.29: Separation and trailing edge wake become parallel downstream of the airfoil.

estimated for 21° is 1.221 obtained from the data where as from the solver it is 1.28. The time step for the above simulations is considered to be 0.1s which is large and hence the wakes are convected downstream quickly to avoid any unphysical interaction with the airfoil and 40 elements are chosen to represent the airfoil. The unusual spike observed after the separation location in the pressure plot is due to the time discretization issue as explained in section 5.3.1. The remainder of the pressure distribution falls close to the distribution obtained from experimental data. The wake formed in such a simulation is given in figure 5.28. The separation wake and trailing edge wake become parallel to

each other downstream of the airfoil when the solution reaches steady state, as expected, shown in figure 5.29.

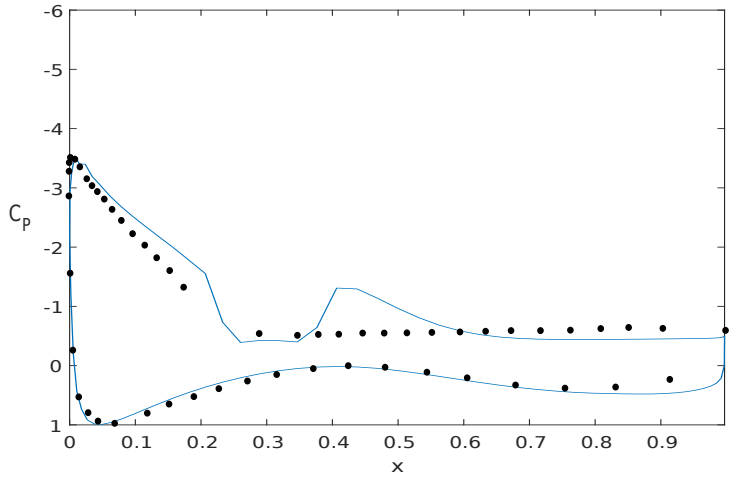

Figure 5.30: C_p distribution at 21° angle of attack. Solid line is obtained from the simulation where as dotted curve is from experiment data taken from [26].

The problem of reattachment is observed in both the vortex methods, discrete and linear distribution panel methods. Since we know that on 2D LEI kite airfoil, flow reattaches on the pressure side behind the leading edge tube. It might be thought that increasing the panel density at the reattachment location could rectify the vortices penetrating the airfoil surface. But even in the case of distribution of vorticity, the problem seem to exist which suggests that increasing panel density might not be a solution to the problem. A similar condition used to model flow separation might have to be formed to model the flow reattachment but such a condition, to the authors knowledge, is not available.

Chapter 6

Conclusions

The steady state models developed in this study are successfully validated and show perfect conformity with similar inviscid models in the literature. The discrete vortex steady state model is validated for the cases of flat plate and cambered plate. In these cases the application of Kutta condition is in built and no specific implementation is required. The lift and moment polars obtained for the flat plate follow the analytical solution identically as shown in figures 5.4, 5.5. In the case of cambered plate, with increase in camber, the analytical solution deviate from the results obtained from steady state model. This is due to the fact that analytical solution is obtained by small disturbance approximations and is applicable only for small camber $e < 0.1$. The deviation of analytical lift and moment polars from steady state results in shown in figures 5.8, 5.9.

The unsteady single wake models for attached flows is validated using the case of impulsively started flat plate. It is observed that at time $t = 0+$, the unsteady lift is high due to fluid acceleration term $\frac{\partial \phi}{\partial t}$. The lift and circulation become asymptotic to the steady state values as the starting vortex convects away. In this state, fluid acceleration term becomes negligible and lift can be accurately predicted with out its inclusion. The circulation shed at the trailing edge becomes insignificant when unsteady solution becomes asymptotic to the steady state value as shown in 5.11. The pressure distribution also reaches close to the steady state distribution with increase in time 5.14. Similar behavior is observed for a impulsively started cambered plate.

The unsteady double wake model developed using discrete vortices in this study couldn't be successfully validated mainly due to uncertainty in the separation wake shedding procedure. The location of separation wake vortex is not exactly known from the literature. Also the location of velocity point that defines the strength of the separation wake is not clearly known. Various attempts of changing theses location within 5% of the chord near the separation location didn't result in a successful model. Other problems without considering the above mentioned modeling issue relate to wake shedding such as wake elements accumulation near the bound vortices on the airfoil and in certain cases wake elements entering the airfoil 5.20 are observed.

In a parallel study using distribution of singularity elements instead of discrete vortex model, also resulted in similar wake shedding issues shown in figure 5.26. Using linear distribution of singularity elements would linearize the equation defining the circulation shed 5.2. This allows to include the unknown of separation wake vorticity into the linear system of equations and can be solved in the current time step. When the separation vortices do not penetrate into the airfoil surface, the pressure distribution seems to be close to the experimental data, which is evident from pressure distribution plot, figure 5.30, obtained for a simulation of airfoil FFA_W3_241 at 21° angle of attack. But when the simulation is performed at angle of attack 17°, the separation wake vortices penetrate into the airfoil surface and the solution becomes unphysical which is evident from the unreasonable pressure distribution plot, figure 5.27. If the time step is increases in an attempt to convect the wake vortices quickly downstream before they penetrate into the surface, it can be expected that pressure distribution would show rapid jumps because of the discretization issue on the time step as discussed in section 5.3.1.

Using discrete vortex elements forces to define the strength of the shed circulation using information from previous time step. But by linearizing the equation defining the strength of wake vortex, allows to include it as an unknown in the linear system of equations. Insight into the criteria for the selection of appropriate time step for double wake model are understood. In a particular time step, the wake elements should not convect more than the distance equal to one panel length. Hence, It is not advisable to discretize the airfoil into higher number of panels which would set a small time step. This significantly increases the computational time.

The objective 2.4 of this thesis is not successfully achieved due to unsuccessful implementation of double wake model. However an expertise in vortex models and the usage of various singularity elements is developed. An insight into identifying the boundary conditions of the problem and choosing singularity element accordingly is achieved.

6.1 Further work

Once the problems mentioned in the modeling of double wake method are solved, the successful model can be easily extended to a 2D LEI kite profile. An additional wake has to be modeled at the pressure surface separation location as shown in figure 6.1 and care must be taken that the wake elements doesn't cross the airfoil or accumulate near it.

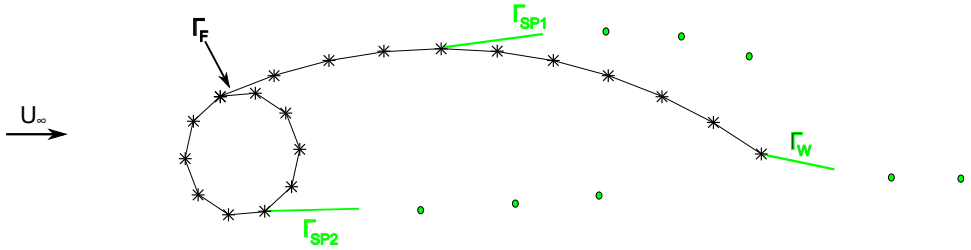

Figure 6.1: Concept sketch of triple wake model for 2D LEI kite airfoil.

Chapter 7

Recommendations

One of the main modeling difficulties faced while developing the double wake model is that the shed wake elements coming close to the bound vortex distribution and cross the airfoil during intermediate time steps. It is found in literature that this is a usual issue faced in unsteady vortex panel methods [35].

The separation wake crossing or coming close to the airfoil can be manually corrected. Correction for the wake elements that are close to the airfoil can be achieved by identifying the wake vortices close to the airfoil and moving them away. A pseudo boundary of particular distance δ has to be created around the airfoil, as shown in figure 7.1. The closest normal distance of wake elements to the airfoil has to be measured and if this distance is less than δ, then the wake elements have to be moved outside the boundary. At every time step, after moving the wake, this correction algorithm can be implemented by estimating the distance of wake elements that are in the vicinity of the airfoil. The effect of variation of the thickness of such a pseudo boundary has to be studied.

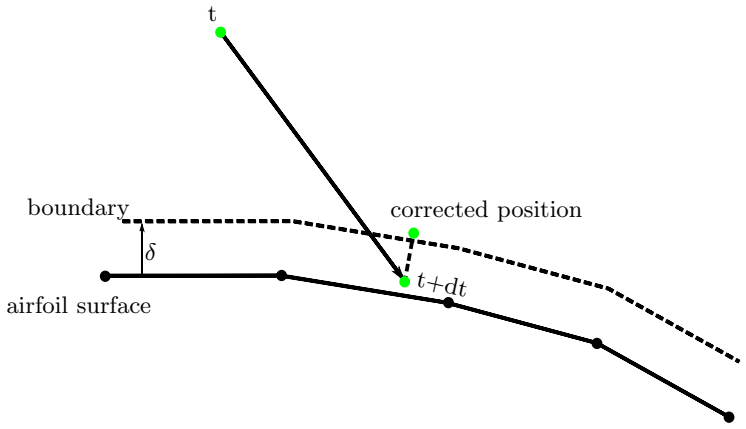

Figure 7.1: Wake elements coming close the airfoil surface that are moved out of the boundary at a distance δ from the airfoil surface.

During intermediate time steps, some wake elements might penetrate through the airfoil surface, as shown in figures 5.20, 5.26. Such a problem is not witnessed in the single wake models because the wake elements are quickly convected downstream and have no chance to interact with the airfoil. One idea is to remove such vortices but this might result in the violating Kelvin's theorem of conservation of circulation. A feasible solution is to manually correct such cases by reflecting the wake elements at the airfoil surface as illustrated in figure 7.2.

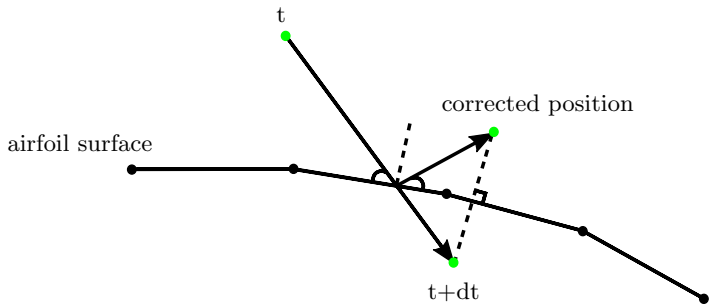

Figure 7.2: Wake element that crosses the airfoil surface and enters inside. Corrected position by reflection from the surface.

References

[1] Pietro Giannattasio Alessandro Zanon and Carlos J. Simo Ferreira. A vortex panel model for the simulation of the wake flow past a vertical axis wind turbine in dynamic stall.

[2] Paolo Tiso Allert Bosch, Roland Schmehl and Daniel Rixen. Nonlinear aeroelasticity, flight dynamics and control of a flexible membrane traction kite. In Uwe Ahrens, Moritz Diehl, and Roland Schmehl, editors, *Airborne Wind Energy*, Green Energy and Technology, chapter 17, pages 307–323. Springer, Berlin Heidelberg, 2013.

[3] Jackson Peter S. Flay Richard G. J. Bailey, Keith I. Modelling viscous flow around 2-d yacht mast and sail configurations. In *13th Australian Fluid Mechanics Conference*, Yacht Research Unit, Department of Mechanical Engineering, University of Auckland, Auckland, New Zealand, 1998.

[4] B. C. Basu and G. J. Hancock. The unsteady motion of a two-dimensional aerofoil in incompressible inviscid flow. *Journal of Fluid Mechanics*, 87:159–178, 1978.

[5] Leonardo Bergami, Mac Gaunaa, and Joachim Heinz. Indicial lift response function: an empirical relation for finite-thickness airfoils, and effects on aeroelastic simulations. *Wind Energy*, 16(5):681–693, 2013.

[6] J. Breukels. *An Engineering Methodology for Kite Design*. PhD thesis, Delft University of Technology, 2011.

[7] A. Bruining. Aerodynamic characteristics of a curved plate airfoil section at reynolds numbers 60.000 and 100.0000 and angles of attack from -10 to +90 degrees. Technical Report LR-281, Delft University of Technology, Delft, Netherlands, 1979.

[8] Antonello Cherubini, Andrea Papini, Rocco Vertechy, and Marco Fontana. Airborne wind energy systems: A review of the technologies. *Renewable and Sustainable Energy Reviews*, 51:1461–1476, 2015.

[9] Michael Deaves. An investigation of the non-linear 3d flow effects relevant for leading edge inflatable kites. Master's thesis, 2015.

[10] R. G. den Boer. Numerical and experimental investigation of the aerodynamics of double membrane sailwing airfoil sections. Technical Report LR-345, Delft University of Technology, Delft, Netherlands, 1982.

[11] EnerKite. Enerkíte – products – ek200. http://www.enerkite.de/en/products.

[12] A. Fage and F. C. Johansen. On the flow of air behind an inclined flat plate of infinite span. *Proceedings of the Royal Society of London A: Mathematical, Physical and Engineering Sciences*, 116(773):170–197, 1927.

[13] Tracy E. Fritz and Lyle N. Long. Object-oriented unsteady vortex lattice method for flapping flight. 41(06).

[14] J. H. Gerrard. Numerical computation of the magnitude and frequency of the lift on a circular cylinder. *Philosophical Transactions of the Royal Society of London A: Mathematical, Physical and Engineering Sciences*, 261(1118):137–162, 1967.

[15] J. L. Hess and A. M. O. Smith. Calculation of potential flow about arbitrary bodies. *Progress in Aerospace Sciences*, 8:1–138, 1967.

[16] Kitemill. http://kitemill.com.

[17] Ampyx Power B.V. http://www.ampyxpower.com/.

[18] Makani Power/Google. http://www.google.com/makani.

[19] KitePower. http://www.kitepower.eu.

[20] Bong-jin Im. A numerical method for the calculation of unsteady lifting potential flow problems, 8 1982.

[21] J. Katz. Large-scale vortex-lattice model for the locally separated flow overwings. *AIAA Journal*, 20(12):1640–1646.

[22] J. Katz. A discrete vortex method for the non-steady separated flow over an airfoil. 102:315–358, 1981.

[23] Joseph Katz and Allen Plotkin. *Low-speed aerodynamics*. Cambridge University Press, 2 edition, 2001.

[24] Richard Leloup. *Modelling approach and numerical tool development for kite performance assesment and mechanical design ; application to vessels auxiliary propulsion.* PhD thesis, 2014.

[25] Rachel C Leuthold. Multiple-wake vortex lattice method for membrane-wing kites. Master's thesis, 2015.

[26] Kenneth Lnbk. Double-wake model for airfoils, 2016.

[27] L Marion, N Ramos-Garca, and J N Sorensen. Inviscid double wake model for stalled airfoils. *Journal of Physics: Conference Series*, 524(1):012132, 2014.

[28] George B. McCullough and Donald E. Gault. Examples of three representative types of airfoil-section stall at low speed. Technical Report NACA TN 2505, NASA, Ames Aeronautical Laboratory, Moffett Field, California, 9 1951.

[29] C Michler. *Efficient Numerical Methods for Fluid-Structure Interaction*. PhD thesis, 2005.

[30] Antoine Cayron N. Ramos-Garca and J. N. Srensen. Unsteady double wake model for the simulation of stalled airfoils. *Journal of Power and Energy Engineering*, 3(7):20–25, 12 2015.

[31] M. Prabu Sai Manoj, Piyush Jadhav D., and Sunetra Sarkar. Quasi-steady fluid structure interaction model of the surf kite. In R. Schmehl, editor, *Book of Abstracts of the International Airborne Wind Energy Conference 2015*, Delft University of Technology, 2015. Delft University of Technology.

[32] N. Ramos-Garca, Hamid Sarlak Chivaee, S. J. Andersen, and J. N. Srensen. Simulation of the flow past a circular cylinder using an unsteady panel method. *Applied Mathematical Modelling*, 12 2016.

[33] T.S.R. Reddy and K.R.V. Kaza. A comparative study of some dynamic stall models. Technical Report NASA-TM-88917, NASA, NASA Lewis Research Center Cleveland, Ohio 44135, 3 1987.

[34] R.H.M. van Kappel. Aerodynamic analysis tool for dynamic leading edge inflated kite models a non-linear vortex lattice method. Master's thesis, 2012.

[35] M. Vezza and R. A. M. Galbraith. An inviscid model of unsteady aerofoil flow with fixed upper surface separation. *International Journal for Numerical Methods in Fluids*, 5:577–592, 6 1985.

[36] Albert E. von Doenhoff and Neal Tetervin. Investigation of the variation of lift coefficient with reynoldsnumber at a moderate angle of attack on a low-drag airfoil. Technical report, NASA, Langley Memorial Aeronautical laboratory, Langley Field, Virginia, 11 1942.

[37] S. Wilkinson. Static pressure distributions over 2d mast/sail geometries. *Mar. Technol.*, 26(4):394–395, 1989.

Chapter 8

Appendix

8.1 Validation of linear distribution vortex panel method

The validation study is performed on symmetrical airfoil NACA 0015 shown in figure 8.1.

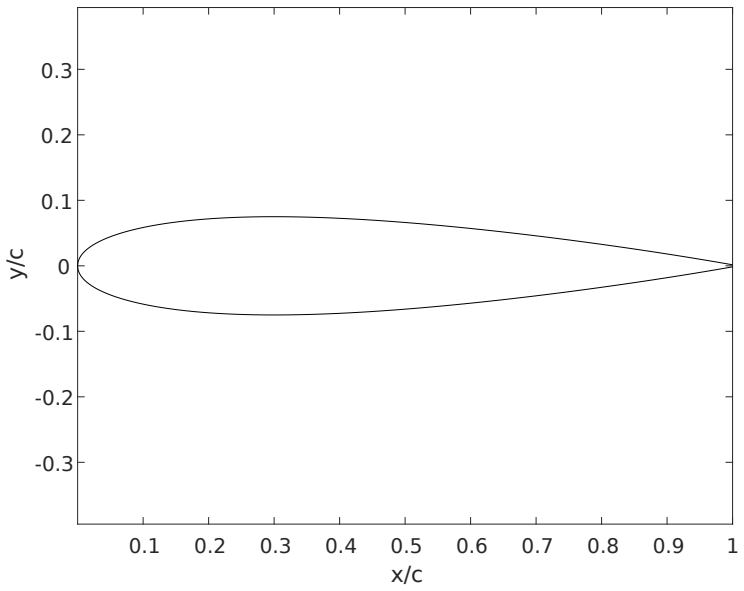

Figure 8.1: Symmetrical airfoil NACA 0015.

8.1.1 Steady state model

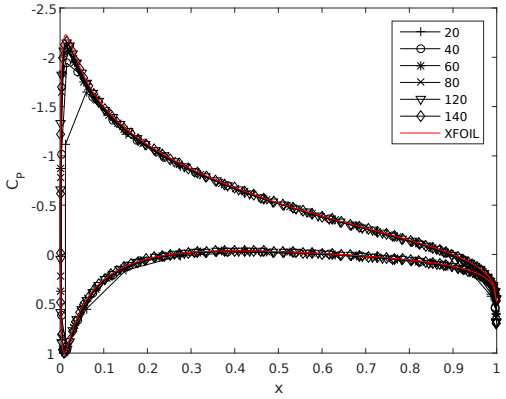

Figure 8.2: Convergence of pressure distribution at $5°$ angle of attack studied for various number of panels.

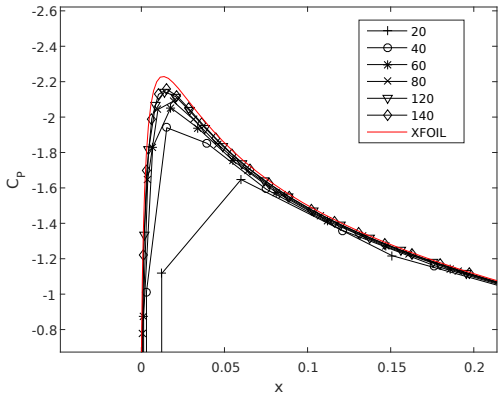

Figure 8.3: Zoom in of pressure distribution at the leading edge.

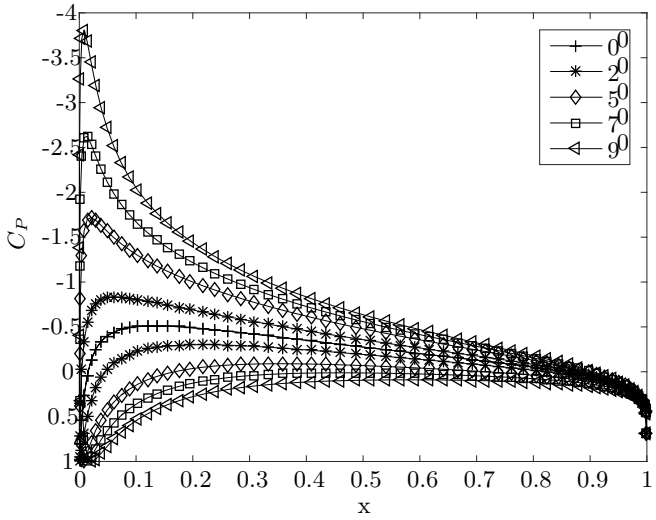

Figure 8.4: Pressure distribution plots for various angle of attacks from the steady state model.

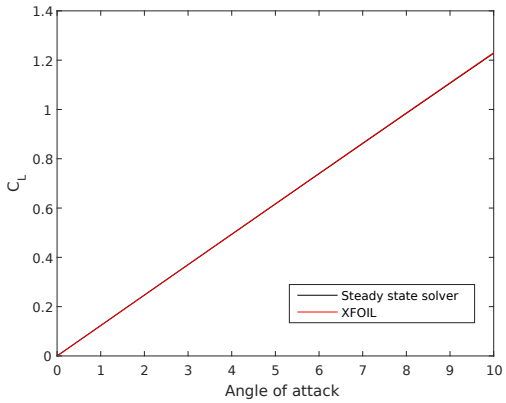

Figure 8.5: Validation of lift polar with corresponding XFOIL results.

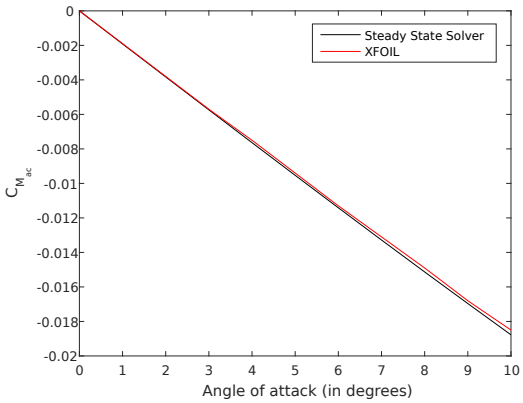

Figure 8.6: Validation of moment polar with corresponding XFOIL results.

8.1.2 Unsteady single wake model for attached flows

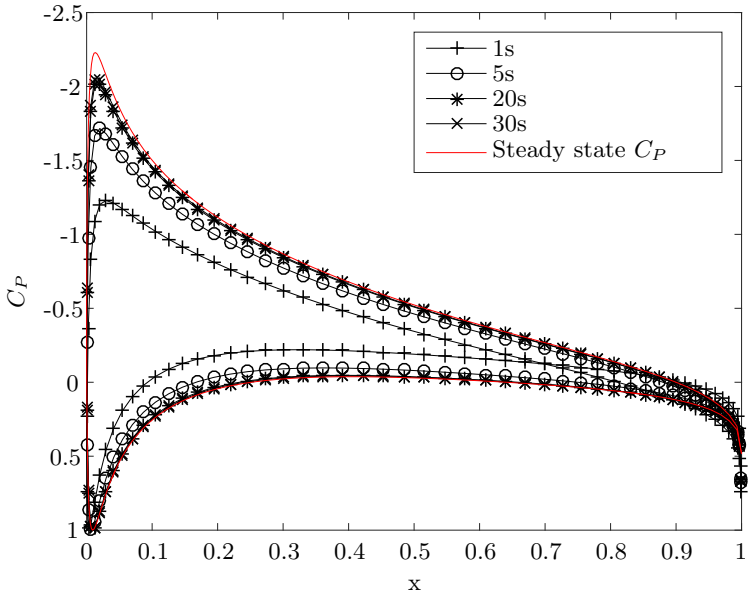

Figure 8.7: Pressure distribution at $5°$ angle of attack approaching the steady state distribution with time.

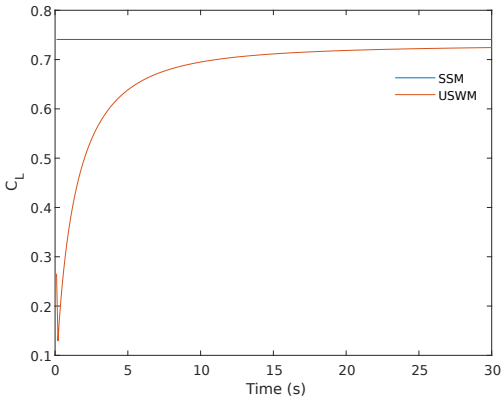

Figure 8.8: Convergence of lift coefficient at 5° angle of attack to the steady state value..

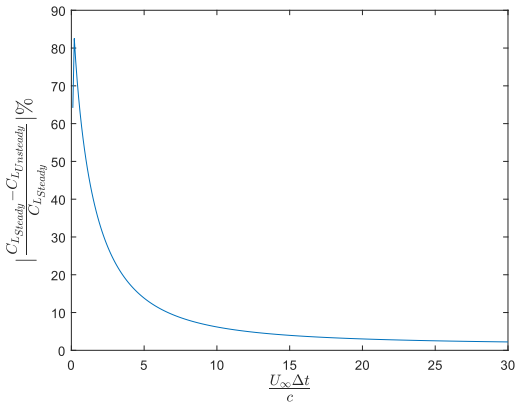

Figure 8.9: Percentage difference between unsteady and steady lift coefficient at 5° angle of attack with time.